Advances in Water Resources 206 (2025) 105108

Contents lists available at ScienceDirect

Advances in Water Resources

journal homepage: www.elsevier.com/locate/advwatres

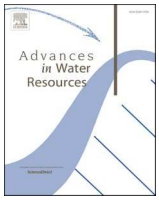

Breaking down annual and tropical cyclone-induced nonlinear interactions in total water levels

Md Shadman Sakib [a], David F. Muñoz [a,*], Thomas Wahl [b]

[a] Department of Civil and Environmental Engineering, Virginia Tech, Blacksburg, VA 24060, United States
[b] Department of Civil, Environmental and Construction Engineering & National Center for Integrated Coastal Research, University of Central Florida, Orlando, FL 32816, United States

ARTICLE INFO

Keywords:
Nonlinear interactions
Total water level
Tropical cyclones
Chesapeake Bay

ABSTRACT

With the increase of tropical cyclone activity, coastal communities will experience growing impacts from extreme water levels and associated compound flooding. Multiple drivers contribute to total water level (TWL), including mean sea level, astronomical tides, riverine flow, storm surges, and waves. Therefore, gaining insight into future TWL variability requires a thorough understanding of how those drivers nonlinearly interact at different spatiotemporal scales. In this study, we developed a coupled coastal and wave model at sufficient spatial resolution to analyze: (i) tide–driver interactions and their nonlinear components stemming from surge, river flow, and wind-waves, and (ii) their spatiotemporal evolution across the pre-landfall, landfall, and post-landfall stages of tropical cyclones in the Chesapeake Bay, USA. Results show that tide–surge and tide–wave interactions, along with their nonlinear components, exhibit substantial annual variability, with extreme hurricanes producing abrupt and spatially distinct responses driven by low pressure anomalies in slow-moving storms and wind setup in faster systems. In contrast, tide–river interactions remain negligible except in the upper bay tributaries. A weak or neutral tide–driver interaction does not necessarily indicate a negligible nonlinear response. Rather, nonlinear interactions (NIs) generally act out of phase with their associated drivers, functioning as compensatory mechanisms that amplify or suppress TWL. These nonlinearities are transient and of high-frequency nature near the coast, but evolve into slower, more persistent fluctuations in upstream regions. As climate change reshapes coastal dynamics, a robust understanding of NIs is essential for designing effective flood protection, enhancing risk assessments, and developing informed adaptation strategies for extreme water levels.

1. Introduction

Coastal regions of the United States are increasingly vulnerable to flooding due to tropical cyclones, which have been responsible for substantial economic losses and fatalities. According to the National Center for Environmental Information (NCEI), the United States has experienced more than 67 tropical cyclones since 1980 that collectively incurred costs of approximately $1.5 trillion and resulted in 7211 fatalities (Smith, 2025). Tropical cyclone-induced flood events can result from multiple interacting drivers, including storm surge, riverine flow, precipitation, astronomical tides, and wave setup. When these drivers occur simultaneously or sequentially, their interactions can amplify flood severity and lead to compound flood (CF) events (Green et al., 2025; Zscheischler et al., 2020). CF events are not simply additive rather their nonlinear interactions (NIs) can amplify or attenuate total water levels (TWLs). However, most operational frameworks treat flood drivers separately and combine them via linear superposition rather than resolving any NIs. For example, NOAA's Probabilistic Tropical Storm Surge model (P-Surge) integrates ensembles of the Sea, Lake, and Overland Surges from Hurricanes (SLOSH) hydrodynamic model forecasts. Rather, tidal signals are calculated separately—often using harmonic constituents derived from models such as ADCIRC—and later added to the surge output in a post-processing step to estimate total water levels through linear superposition (Haase et al., 2012; Penny et al., 2023). Furthermore, as predicting the exact timing of peak storm surge relative to tidal cycles remains relatively challenging, forecasters prefer to use SLOSH model outputs without embedded tidal components (Glahn et al., 2009). Similarly, U.S. Army Corps of Engineers' North Atlantic Coast Comprehensive Study (NACCS), which is a large-scale regional study, adopts a linear superposition framework (combining

* Corresponding author.
E-mail address: davidmunozpauta@vt.edu (D.F. Muñoz).

https://doi.org/10.1016/j.advwatres.2025.105108
Received 15 April 2025; Received in revised form 1 September 2025; Accepted 1 September 2025
Available online 2 September 2025

tides, storm surge, and sea level rise) to generate over 1000 synthetic cyclone response (Nadal-Caraballo et al., 2015). Across these operational methods (e.g., P-Surge/SLOSH) or planning assessments (e.g., NACCS) computational efficiency and timeliness are always prioritized and, in both cases, explicit resolution of NIs is absent. Therefore, while recent research efforts have explored the nonlinear interactions among surge, waves, and tides (Tien et al., 2025) or between rainfall, river discharge and surge (Li et al., 2023; Sarhadi et al., 2024; Xu et al., 2025) these advanced approaches are yet to be fully integrated into routine operational frameworks. As a result, current simplified practice often fails to capture the NIs that can occur among flood drivers during extreme weather events (Bilskie and Hagen, 2018; Moftakhari et al., 2017; Reed et al., 2015). Furthermore, both short-term (intra-annual) and long-term (inter-annual) climate variability, e.g., El Niño and La Niña, can substantially alter atmospheric pressure anomalies and wind patterns (Haigh et al., 2014; OrtizBeviá et al., 2010; Serafin et al., 2017). These climatic shifts add another layer of complexity to the already intricate NIs between CF drivers.

In coastal systems, the tide-surge interaction (TSI) is a key nonlinear process between tidal forces and storm surges that can considerably alter coastal hydrodynamic responses and elevate associated flood hazards. TSI is particularly pronounced in shallow coastal regions and estuaries, where the combined effects of tides and surges result in nonlinear responses that either amplify or attenuate water levels (Xiao et al., 2021). The nonlinear nature of TSI arises from the timing and magnitude of tide and storm surge peaks, which can coincide or diverge, leading to variations in the overall water level experienced at the coast (Feng et al., 2018; Yin et al., 2022). Studies have shown that a positive surge can increase the phase speed of tidal propagation, altering the timing of tidal high water. This effect is particularly critical for flood hazard during spring tide conditions combined with large, positive surges (Lyddon et al., 2018; Pinheiro et al., 2020). In contrast, during low tide conditions, the same surge can lead to heightened water levels, demonstrating the dual nature of TSI effects (Huang et al., 2024). For instance, the timing of storm surges relative to tidal cycle has a considerable effect on flood hazard assessments, indicating that TSI can either exacerbate or mitigate flood hazards depending on site-specific conditions (Lyddon et al., 2018).

Wind waves that propagate parallel to or against the tidal currents can modify the energy distribution and phase relationships, leading to variations in tidal amplitudes and potentially increasing flood risk (Bolaños et al., 2013; Xing et al., 2012). Using Hurricane Floyd (1999) as a case study, Funakoshi et al. (2008) demonstrated that one- and two-way coupling of SWAN+ADCIRC captured wave contributions of 10–15 % to storm tide elevations via radiation stress gradients. Dietrich et al. (2010) developed a tightly coupled SWAN+ADCIRC system on a shared unstructured mesh that showed wave radiation stresses increased water levels by approximately 0.7–0.8 m during Hurricane Katrina (2005), amounting to 25 %–35 % of the total peak surge in Mississippi River delta, Grand Isle, and other barrier islands southeastern Louisiana. Along the U.S. Atlantic and Gulf coasts wind driven setup is a key contributor to peak storm tides, particularly in coastal regions with narrow continental shelves such as the southeastern coast of Florida and the southern Mississippi River Delta (Marsooli and Lin, 2018). In that study, the authors reported that the largest wave setup contribution reached approximately 0.46 m, accounting for 50 % of the peak surge at North Miami Beach, Florida, during Hurricane Andrew in 1992. Similarly, during Typhoon Soudelor in 2015, the surge driven by pure wave radiation stress reached 0.55 m at Suao Port, Taiwan, due to offshore wind-waves exceeding 16 m (Chen et al., 2017). Beyond the immediate impacts on flooding, the long-term changes to wave climate and wind patterns can alter the frequency and intensity of storm events, ultimately affecting the broader coastal flooding dynamics (Jiang et al., 2016; Semedo et al., 2012; Vitousek et al., 2017).

As tides propagate landward into estuaries, tide-river interaction (TRI) leads to tidal asymmetry and alters the timing and magnitude of high and low tides. Here, the quadratic bottom friction is the primary dissipative force that reduces tidal wave energy as it moves upstream (Dronkers, 1986; Fagherazzi et al., 2003). Studies have shown that these frictional effects are particularly pronounced in shallow estuarine environments, where the bed friction coefficient can vary with sediment type and flow conditions (Cai et al., 2014; Valle-Levinson et al., 2000). For example, low river flow regimes induce notable phase lag in tidal propagation due to frictional influences in the lower reaches of the Guadalquivir River estuary in Spain (Losada et al., 2017). This phase lag, which can reach up to $\pi/4$, alters the timing and amplitude of tidal waves as they interact with river flow. The amplification and dampening of water levels in estuaries are also influenced by the spatial and temporal variability of river flow. This effect is particularly pronounced in estuaries with substantial freshwater inflow, where the tidal range can vary drastically between dry and wet seasons such as in the Yangtze River, China (Guo et al., 2015). Similarly, the spatial distribution of quarter-diurnal tide and their dissipation shift in response to seasonal discharge patterns in the Ganges-Brahmaputra-Meghna delta (Elahi et al., 2020). This, in turn, influences total friction in the upper tidal basin.

Existing studies generally focus on the aggregate tide–driver response, with limited effort to isolate and contrast their nonlinear contributions, leaving a gap in understanding how these interactions evolve in space and time. In this study, we isolate these NIs to explicitly characterize their independent behavior. Using the Chesapeake Bay as a representative case of a large and hydrodynamically complex estuarine system, we examine how these NIs respond to three physically distinct tropical cyclones i.e., Sandy (2012), Irene (2011), and Isabel (2003). These storms differ in trajectory, intensity, translational speed, and duration, offering a robust testbed for comparative analysis. In addition to analyzing storm-specific extreme responses, this study explicitly examines their spatiotemporal behavior across the full annual cycle. This allows us to establish a critical baseline for identifying when and where nonlinear dynamics emerge as dominant contributors to total water level variability. This leads to two central research questions: (i) How do NIs and their corresponding total tide–driver responses co-evolve and diverge spatiotemporally across the pre-landfall, landfall, and post-landfall stages of tropical cyclones? and (ii) Do these patterns persist across storms with contrasting dynamic characteristics? To this end, our study presents a dual perspective: it examines NIs relative to their total interaction effects and compares their behavior during extreme events to typical annual variability, providing a more nuanced understanding of how coastal systems respond to both routine and extreme hydrodynamic forcing.

2. Study framework

2.1. Study area

The Chesapeake Bay is the largest estuary in the United States and one of the most diverse coastal ecosystems of the world (Fig. 1a). The bay is situated on the western side of the Delmarva Peninsula between Virginia (VA) and Maryland (MD) and spans approximately 11,400 km^2. The bay extends in a north-south direction from Virginia Beach, VA, to Havre de Grace, MD, where it meets the Susquehanna River's mouth (Colman and Mixon, 1988). With an average depth of 6.5 m (Patrick, 1994), this relatively shallow bay spans approximately 315 km in length and has a varying width ranging from 6.4 km to 48 km near Annapolis, MD, and Cape Charles, VA, respectively. Freshwater inflow to the bay comes from a network of nearly 50 rivers and thousands of tributary streams which collectively drain an area of approximately 166,000 km^2. Among these, three major rivers contribute more than 80 % of the Chesapeake Bay's total freshwater inflow, namely the Susquehanna, the Potomac, and the James rivers (Table 1). The Susquehanna River alone accounts for nearly half (49 %) of the freshwater inflow to the bay (Xiong and Berger, 2010). The mean tidal range along the Chesapeake

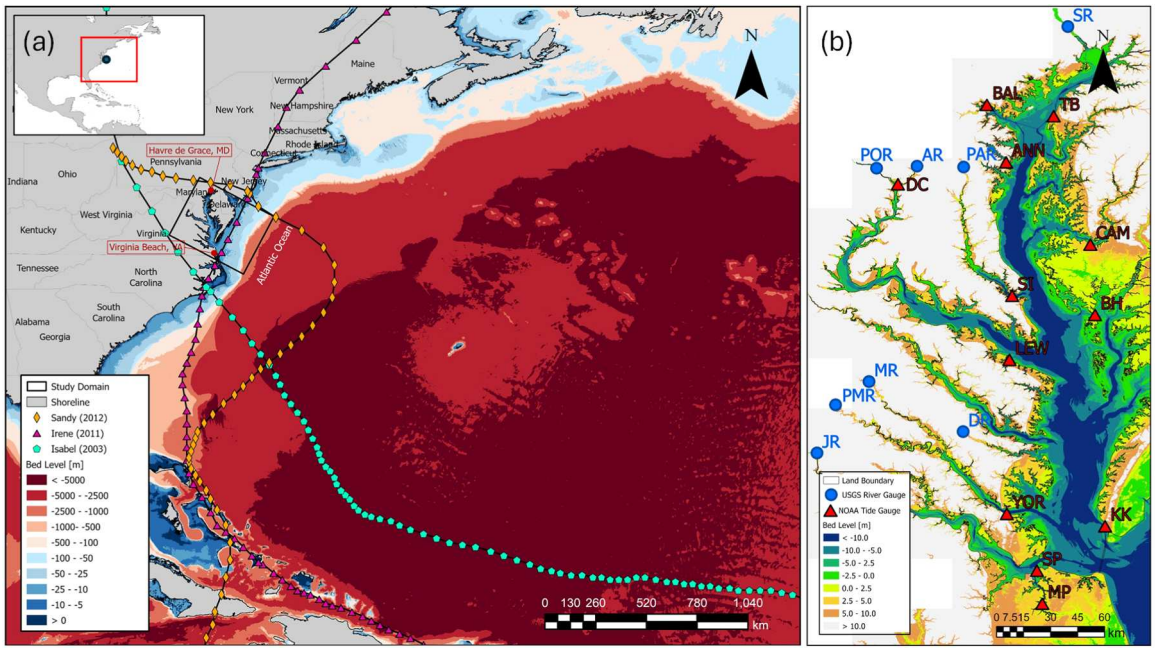

Fig. 1. Map of the study area showing the Chesapeake Bay, VA-MD and the U.S. Atlantic Ocean. (a) Spatial extent of the Atlantic Ocean model with the underlying bathymetry obtained from GEBCO 2024, and the National Hurricane Center's best tracks of Sandy (Oct/2012), Irene (Aug/2011), and Isabel (Sep/2003). (b) Spatial extent of the Chesapeake Bay model with the underlying bathymetry obtained from NOAA's lidar surveys. Blue dots represent USGS river-gage stations serving as upstream boundary conditions whereas red triangles indicate NOAA tide-gage locations used for model calibration and validation. Abbreviations of station codes shown on the map correspond to those listed in Table 1.

Bay varies considerably, with values of 0.78 m near the bay's entrance (NOAA 8638863), 0.30 m at Annapolis, MD (NOAA 8575512), and 0.37 m at Tolchester Beach, MD (NOAA 8573364) (Zhong and Li, 2006). The tides are predominantly semi-diurnal, dominated by the principal lunar semidiurnal (M2) and the larger lunar elliptic semidiurnal constituent (N2), with tidal amplitudes of 1.26 m and 0.28 m, respectively.

2.2. Hurricane events

We simulate annual TWL variability and break down NIs from three selected hurricanes that impacted Chesapeake Bay, namely Hurricane Sandy from 2012, Hurricane Irene from 2011, and Hurricane Isabel from 2003 (Fig. 1a). Hurricane Sandy made landfall as a Category 1 hurricane on the Saffir-Simpson scale just northeast of Atlantic City, New Jersey, USA. Hurricane landfall occurred at approximately 23:00 UTC on October 29, 2012, with maximum sustained winds of 129 km/h (Bennett et al., 2018). Storm surge in New York City coincided with the approximate timing of the spring high tide, resulting in a record-breaking TWL of 4.23 m at The Battery in New York Harbor (Blake et al., 2012). High water levels along the Delaware River in Philadelphia reached 3.24 m early on October 30, 2012, whereas waves generated by strong winds were recorded at over 6.40 m at southern Lake Michigan (Blake et al., 2012; NOAA, 2012). In the United States, the storm caused an estimated $88.5 billion in damages, making it the most devastating Category 1 storm in history and the fifth costliest storm overall in the country (Smith, 2025).

Hurricane Irene originated from a tropical wave off the west coast of Africa. On August 24 at 12:00 UTC, it reached the Bahamas and intensified into a Category 3 hurricane on the Saffir-Simpson Scale, with a peak sustained wind speed of nearly 195 km/hr. It made its primary landfall as a Category 1 hurricane on the North Carolina shoreline in the US at 12:00 UTC on August 27, 2011. It made a second landfall near New Jersey at 09:35 UTC on August 28, 2011, before continuing its path along the Atlantic coastline As Hurricane Irene transitioned to an extratropical cyclone, it triggered heavy rainfall that caused catastrophic river flooding in New York, New Jersey, and the Delaware River region, resulting in nearly $1 billion in damages (Deb et al., 2023; Kerns and Chen, 2023; Lixion and Cangialosi, 2011). It generated large waves along Outer Banks barrier islands in North Carolina and moved through the Albemarle-Pamlico estuarine system causing widespread flooding, and extensive erosion across the low-lying coastal plain (Mulligan et al., 2008, 2015). Post-storm surveys showed storm surge of approximately 2.4 to 3.4 m occurred in parts of Pamlico Sound, while surge values ranging from 1.2 to 1.8 m along the coastline from New Jersey, US (Lixion and Cangialosi, 2011).

Hurricane Isabel originated from a tropical wave in the far eastern Atlantic, reaching Category 5 strength on the Saffir-Simpson Scale around September 11, 2003. It maintained its peak intensity until September 15 before making landfall as a Category 2 hurricane near Drum Point, North Carolina, at 17:00 UTC on September 18, 2003, with sustained winds of around 160 km/hr (NOAA, 2004b; Preller et al., 2003). The highest surge height was recorded in Chesapeake City, MD, where it reached 2.49 m on September 19, 2003. Water levels exceeding 2 m were observed in Washington, DC, Baltimore and Tolchester Beach, MD. The U.S. Army's Field Research Facility at St. Petersburg recorded a significant wave height of 8.1 m at a waverider buoy located in 20 m of water (Lin et al., 2010; NOAA, 2004a; Xiao et al., 2021). According to the National Weather Service Assessment (2004b), Hurricane Isabel resulted in 51 fatalities, including 17 directly attributed to the storm, and caused an estimated $3.37 billion in damages.

2.3. Data sources

We use publicly available data to set up, calibrate, and validate coastal hydrodynamic and wave models of the Chesapeake Bay and the Atlantic Ocean. To represent physical topography and bathymetry (topobathy), we consider datasets from NOAA's Continuously Updated Digital Elevation Model (CUDEM). These data cover the Chesapeake Bay region with a 1/9 arc-second resolution (~3.5 m) and are available at https://doi.org/10.25921/ds9v-ky35. We also consider data from the NCEI's Coastal Relief Model that covers the nearshore and coastal regions with a 1/3 arc-second (~10 m) and 1 arc-second (~30 m)

Table 1
River- and tide-gauge stations of Chesapeake Bay.

Region	Station	Code	Station ID	Objective
Lower bay	Sewells Point, VA	SP	NOAA 8638610	Calibration and Validation
	Money Point, VA	MP	NOAA 8639348	
	Kiptopeke, VA	KK	NOAA 8632200	
	Yorktown, VA	YOR	NOAA 8637689	
Mid bay	Cambridge, MD	CAM	NOAA 8571892	
	Lewisetta, VA	LEW	NOAA 8635750	
	Solomons Island, MD	SI	NOAA 8577330	
	Bishops Head, MD	BH	NOAA 8571421	
Upper bay	Baltimore, MD	BAL	NOAA 8574680	
	Tolchester Beach, MD	TB	NOAA 8573364	
	Annapolis, MD	ANN	NOAA 8575512	
Upstream	James River, VA	JR	USGS 02037500	Boundary Condition
	Anacostia River, MD	AR	USGS 01649500	
	Pamunkey River, VA	PMR	USGS 01673000	
	Rappahannock River, VA	RR	USGS 01668000	
	Potomac River, DC	POR	USGS 01646500	
	Susquehanna River, MD	SR	USGS 01578310	
	Choptank River, MD	CR	USGS 01491000	
	Dragon Swamp, VA	DR	USGS 01669520	Internal Discharge
	Patuxent River, MD	PAR	USGS 01594440	
	Mattaponi River, VA	MR	USGS 01674500	

resolution, respectively. This dataset is available at https://www.ncei.noaa.gov/products/coastal-relief-model. Next, we leverage the General Bathymetric Chart of the Oceans (GEBCO) with a 15 arc-second resolution (~500 m) in regions with depths greater than 300 m. This dataset is available at https://www.gebco.net/data_and_products/gridded_bathymetry_data/. The model's vertical datum is referenced to the North American Vertical Datum of 1988 (NAVD88). All topobathy datasets were converted to NAVD88 using NOAA's V-datum program (Tolkova et al., 2023).

Likewise, we consider land cover maps derived from the National Land Cover Database (NLCD) as a proxy for spatially distributed roughness values coinciding with the year of Hurricane Sandy, Irene, and Isabel (https://www.mrlc.gov/data/). The NLCD maps have a 30 m spatial resolution and 16 land cover classes over the continental US. For calibration purposes, the 16 classes were consolidated into 5 broader categories to avoid too much specificity: open water, forest, bare land, urban/impervious areas, agricultural lands, and wetlands.

Open boundaries for the Atlantic Ocean model (Fig. 1a) were forced by using barotropic tides obtained from TPXO 8.0 global inverse tide model (https://www.tpxo.net/global/tpxo8-atlas) whereas sea surface wind fields and atmospheric pressure data of 1 h resolution were sourced from the National Centers for Environmental Prediction's Climate Forecast System Version 2 (CFSv2) at 0.20° (~22 km). River discharge data was used as upstream boundary condition for the Chesapeake Bay model (Fig. 1b) at 11 USGS river-gauges (Table 1; https://dashboard.waterdata.usgs.gov/app/nwd/en/). The downstream boundary condition was obtained by extracting TWL outputs from the Atlantic Ocean Model along an offshore boundary transect approximately 20 km (Fig. 2) off the Chesapeake Bay shoreline. In addition, we forced the Chesapeake Bay model using sea surface wind fields and atmospheric pressure from ERA5 reanalysis data with a temporal resolution of 1 h. Importantly, we noticed that CFSv2 considerably overestimated hurricane-induced wind speed velocities in the upper bay compared to the observed wind data from 20 National Data Buoy Center (https://www.ndbc.noaa.gov/) coastal and inland stations (supplementary Figure S5).

3. Methods

3.1. Model development

We simulate TWL in the U.S. Atlantic Ocean and the Chesapeake Bay using the coupled Delft3D (2D depth-average mode) and Simulating WAves Nearshore (SWAN) model software. These models have extensively been used for simulating storm surge and waves triggered by tropical cyclones and typhons across various coastal regions worldwide (Bakhtyar et al., 2020; Hasan Tanim and Goharian, 2021; Höffken et al., 2020; Muñoz et al., 2022, 2024; Wijetunge and Neluwala, 2023). Delft3D is a versatile 2D/3D modeling suite designed to simulate complex hydro-morphological interactions between river, estuarine, and coastal processes (Deltares, 2018a, 2023). Delft3D includes a structured mesh capability in Delft3D-FLOW (v4.04.01) and an unstructured flexible mesh (FM) capability in Delft3D-FM (v2023.02), which helps conduct hydrodynamic simulations in complex morphological settings with higher accuracy than that of a structural mesh (Kumar et al., 2009). Furthermore, the modeling suite includes a wave module in Delft3D-WAVE that can be coupled with the advanced SWAN kernel to simulate wave dynamics in deep-ocean and nearshore environments (Deltares, 2018a, 2018b, 2023). A schematic diagram illustrating the coupled modeling framework and boundary condition exchange is provided in Fig. 2. More details of the Delft3D and SWAN software packages are included in the Supplementary material.

3.1.1. Atlantic ocean model (AOM)

To optimize runtime efficiency and reduce computational burden, we developed a structured Delft3D-FLOW model of the Atlantic Ocean characterized by low to medium bathymetric complexity (Fig. 1a). The model domain covers a large portion of the ocean to accurately capture the wind field gradient and offshore wind patterns within longitudes and latitudes ranging from 99°W to 20°E and 14°N to 52°N, respectively. This model has a structured grid consisting of 253,259 rectilinear cells and a mesh resolution that gradually increases from 17.5 km in the deep ocean to 2 km near the coastline. Nearshore dynamics were accounted for by applying a progressively finer mesh resolution along the offshore boundary of the Chesapeake Bay model, thereby ensuring accurate representation of coastal processes. In particular, the Atlantic Ocean model helps simulate tide and wind-wave water levels consistent with hurricane's best tracks from the National Hurricane Center.

Next, the Atlantic Ocean model is dynamically coupled with an analogous Delft3D-WAVE (SWAN) model to account for both the effect of wind-waves on current and the effect of flow on waves. To ensure a spatially smooth model coupling, we use an identical structural grid to run both the flow and wave models. First, the Delft3D-FLOW model computes water levels, currents, and wind velocities at each computational node of the numerical mesh. Then, the model outputs are passed on to SWAN with a 30 min coupling interval to calculate wave height, period, direction, and spectral energy distribution. Once SWAN completes the wave simulations, it returns radiation stress gradients to Delft3D-FLOW. These gradients act as a forcing term in the hydrodynamic equations and transfer momentum from waves to the water column. Lastly, Delft3D-FLOW integrates wave-induced forces to update water levels and flow velocities for the next timestep.

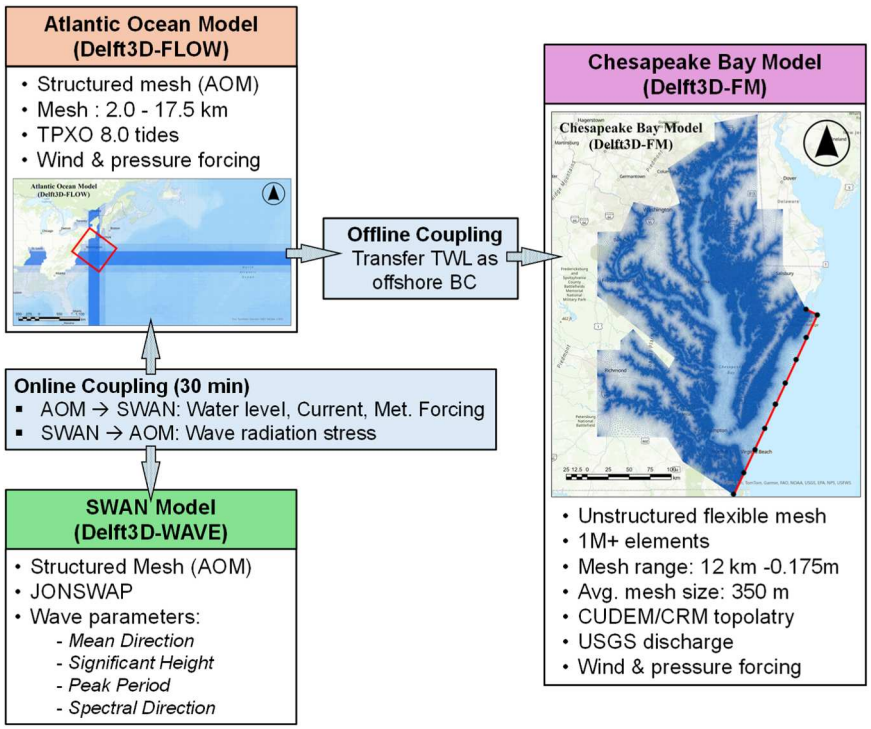

Fig. 2. Schematic of the coupled modeling framework: Atlantic Ocean Model (AOM) is online coupled with SWAN to exchange water levels, currents, meteorological forcing, and wave radiation stress. Offline coupling transfers nearshore TWL output from AOM as offshore boundary input to the high-resolution Chesapeake Bay Model. The red transect denotes the Bay model's downstream boundary, and black dots indicate TWL input locations.

The Smith & Banke (1975) two-breakpoint wind-drag model is applied to the model coupling to translate wind speed into wind-induced stress on the water surface. This is critical to simulate wind setup/wave growth along coastlines in order to capture the nonlinear dynamics of energy transfer from the atmosphere to hydrodynamics. Here, the wind-drag coefficient (C_d) is defined by two-breakpoints – 0.00063 at 0 m/s and 0.00723 at 100 m/s. C_d increases linearly between these thresholds, however, it remains constant beyond the upper breakpoint of 100 m/s, indicating a physical saturation limit where aerodynamic forces stabilize despite further increases in wind speed. Horizontal eddy viscosity and diffusivity is set to 0.1 m^2/s. Depth-induced breaking is modeled using the Battjes and Janssen (1978) formulation, with $\alpha = 1.0$ to control dissipation rates and $\gamma = 0.73$ the threshold for wave breaking based on wave height-to-depth ratios. Bottom friction is parameterized using the JONSWAP formulation, with a friction coefficient of 0.067 m^2/s^3 to account for energy loss due to seabed roughness (Hasselmann et al., 1973). In addition, the model accounts for refractive propagation due to current and depth, energy dissipation due to white-capping (Komen et al., 1984)and non-linear wave-wave interactions including both quadruplets and triads.

3.1.2. *Chesapeake Bay model*

Next, we set up a detailed coastal hydrodynamic model of the Chesapeake Bay in Delft3D-FM. The model has a spatial resolution ranging from 12 km in deeper offshore regions to 500 m over natural floodplains and coastal wetlands (Fig. 1b). In particular, unstructured grids provide a greater flexibility to simulate fine-scale water level dynamics in sinuous and braided river waterways, coastal wetlands, harbors, and urbanized zones like those present in the Chesapeake Bay (Lin et al., 2010; Muñoz et al., 2020; Xiao et al., 2021). The flexible mesh consists of 1067,531 triangle elements and 534,560 nodes and is generated with the OceanMesh2D toolkit, which consists in an open-source MATLAB code for developing optimized 2D unstructured meshes for coastal and ocean modeling (Roberts et al., 2019). Here, the edge length of the mesh (EL) is controlled by adaptive edge-length function based on factors such as proximity to shorelines, feature width, bathymetric elevation/slopes, and tidal wavelengths. Moreover, EL is designed to transition from coarse to fine in critical areas (e.g., wetlands, inter-tidal zones); thus, ensuring an accurate representation of dynamic coastal and riverine processes (See more details in the Supplementary material). The Susquehanna, Potomac, James, Anacostia, Pamunkey, and Rappahannock river are set as upstream boundary conditions whereas the remaining river tributaries with relatively low flow rates are modeled as localized inflow sources (Table 1). This approach is adopted to circumvent errors in the underlying DEM data associated with small river tributaries. The connection between the Atlantic Ocean Model and the Chesapeake Bay Model is implemented through offline coupling. Following completion of the annual Atlantic simulations, TWL output at the Bay's mouth (Fig. 2) is extracted and applied as the offshore boundary condition (BC) for the high-resolution Chesapeake Bay Model. The timestep is governed by the Courant-Friedrichs-Lewy (CFL) condition, with a maximum value of 0.7, and model outputs are generated at hourly intervals.

The model demonstrates strong performance across Chesapeake Bay during event-based calibration for Hurricane Sandy (2012). In the upper bay (ANN, TB, BAL), the model shows high accuracy with an average MAE of 0.11 m, RMSE of 0.14 m, NSE of 0.70, and KGE of 0.82. TB station performs best with the lowest MAE (0.10 m) and highest KGE (0.85). In the middle bay, performance is acceptable (average NSE of 0.53, KGE of 0.71), with BH and CAM showing particularly strong results. LEW shows the weakest metrics in this region. In the lower bay (SP, MP, KK, YOR), the model performs best overall, with an average NSE of 0.79 and KGE of 0.76. KK, SP, and YOR show strong conformity to the observation data, while MP has slightly higher errors and lower KGE. The model was validated against two extreme events: (i) Hurricane Irene (2011) and (ii) Hurricane Isabel (2003). During Hurricane Irene, the model shows strong agreement with observed TWL variability. Especially in the lower bay (avg. MAE: 0.14 m, NSE: 0.79), though KGE values remain low, which indicates phase mismatches. The middle bay shows moderate agreement (avg. NSE: 0.51), while upper bay stations

experience lower KGE values, likely due to wind field inaccuracies. For Hurricane Isabel, model performance improves notably, especially in the upper bay (avg. NSE: 0.90), with accurate peak timing, height, and phase alignments. The lower bay maintains strong performance (avg. NSE: 0.85, KGE: 0.76), and the middle bay shows consistent results (avg. NSE: 0.80, KGE: 0.53). Overall, the calibrated model effectively simulates TWL dynamics, particularly for Isabel, with robust phase and amplitude agreement across most stations. Further details of the calibration and validation procedures are available in the Supplementary Material.

3.2. Model scenarios

To investigate the spatiotemporal variability of NIs among tide, storm surge, waves, and river flow, we designed eight numerical scenarios (Table 2). The scenarios allow us to systematically isolate and quantify individual forcing contributions and associated NIs, providing deeper insights into their synergistic behavior. Importantly, each scenario simulates the full annual cycle corresponding to a specific hurricane year i.e., 2012 for Sandy, 2003 for Isabel, and 2011 for Irene, allowing us to capture the long-term buildup of seasonal dynamics and the evolution of NI patterns leading up to the extreme event. The first scenario (S1) serves as the baseline condition where the model is forced solely by astronomical tides at the downstream boundary, with no meteorological or hydrological forcing. Wind forcing, atmospheric pressure, and river flow are entirely excluded, ensuring that the simulation represents a purely tidally driven system. In the second scenario (S2), the model is forced with spatiotemporally varying wind and pressure fields to capture the influence of wind-driven stress and barometric fluctuations on water levels. However, river flow remains inactive, thereby isolating the contributions of wind and pressure-driven surge. The third scenario (S3) isolates the interaction between tidal forcing and freshwater discharge by activating river flow at the upstream boundary while keeping both the wind and pressure forcing turned off. In the fourth scenario (S4), wind forcing is introduced to a tidally driven system without barometric pressure variations (e.g., atmospheric pressure is held constant). This allows us to isolate the effect of wind-induced waves in the absence of pressure-driven surge. The last scenario (S5) incorporates all major forcing simulations including tide at the downstream boundary, storm surge driven by wind stress and pressure variation, and river inflow from the upstream boundary. To isolate and quantify the nonlinear component, three additional scenarios were developed. The sixth scenario (S6) simulates a surge-only system by applying spatially varying wind and atmospheric pressure fields while excluding tidal and riverine inputs. In the seventh scenario (S7), only river flow is activated at the upstream boundary, with no influence from tides, wind, or pressure. This allowed us to isolate the effect of freshwater discharge. Finally, the eighth scenario (S8) represents a pure wind-wave case where only wind forcing is applied over a constant atmospheric pressure field (e.g., 1013 mb), with tides and river inflows deactivated in the system.

Table 2
Model scenarios for analyzing nonlinear interactions of tide, storm surge, wave, and river flow.

Scenario ID	Downstream Boundary	Upstream Boundary	Spatial Wind Forcing	Spatial Pressure Forcing	Wave Effects
S1: Tide Only	Tides	Off	Off	Off	Off
S2: Tide + Storm Surge	Tides	Off	On	On	Off
S3: Tide + River Flow	Tides	River Flow	Off	Off	Off
S4: Tide + Wind Wave	Tides	Off	On	Constant/ 1013 mb	On
S5: Tide + All Forcing	Tides	River Flow	On	On	On
S6: Surge Only	Off	Off	On	On	Off
S7: River Flow Only	Off	Off	Off	Off	On
S8: Wind Wave Only	Off	Off	On	Constant/ 1013 mb	On

In this study, we use the differences in water levels (ζ) between various model run scenarios (Table 2) as a proxy for the tidal contribution and its interaction with other dynamic forcings, such as storm surge, river discharge, and wind-induced waves. While NIs can manifest in multiple ways, the difference in water levels provides a practical and interpretable means to represent the integrated effects of multiple interacting drivers. This allows us to capture the spatiotemporal behavior of NI and identify regions where these complex interactions lead to dampened or highly amplified system response. This approach is consistent with prior studies (Bernier and Thompson, 2007; Horsburgh and Wilson, 2007; Tang et al., 1996; Wankang et al., 2019; Xiao et al., 2021; J. Zheng et al., 2017; P. Zheng et al., 2020).

Subtracting water levels between S1 and S2 simulations allows us to estimate the combined effect of Storm Surge (SS) and Tide-Surge Interaction (TSI), expressed as $\zeta_{TSI+SS} = \zeta_{S2} - \zeta_{S1}$. Similarly, the combined effect of River Flow (RF) and Tide-River Interaction (TRI) is estimated as $\zeta_{TRI+RF} = \zeta_{S3} - \zeta_{S1}$., and the combined effect of Wind Wave (WW) and Tide-Wind Wave Interaction (TWI) is calculated as $\zeta_{TWI+WW} = \zeta_{S4} - \zeta_{S1}$. The effect of NI is inherently embedded within this combined response, as the resulting water level difference reflects both the additive and interactive effects of the tide and the respective driver. Lastly, the combined effect of all forcings (SS + RF + WW) and their associated nonlinear interactions is captured by $\zeta_{TRSWI} = \zeta_{S5} - \zeta_{S1}$. Hereinafter, this fully integrated interaction will be referred to as Net_NI. In order to quantify the nonlinear interaction components (e.g., nonlinear Tide-Surge Interaction, or nTSI), we subtracted the pure contributions of individual forcings (i.e., surge, river flow, and wind-induced waves) from the corresponding combined responses (i.e., TSI + SS, TRI + RF, and TWI + WW). For instance, *nTSI* was calculated as: $nTSI = \zeta_{TSI+SS} - \zeta_{S6}$. We extended this framework to other forcing combinations to calculate the nonlinear Tide-River Interaction ($nTRI = \zeta_{TRI+RF} - \zeta_{S7}$) and Tide-Wind Wave Interaction ($nTWI = \zeta_{TWI+WW} - \zeta_{S8}$) components.

3.3. Generalized approach to define hurricane stages

Hurricanes Sandy - 2012, Irene - 2011, and Isabel - 2003 triggered distinctive system's response, driven by variation in each hurricane's intensity, trajectory, translational speed, and duration. For instance, Hurricane Sandy was a relatively slow-moving event that had an expansive wind field (Blake et al., 2012). Hurricane Irene was a more compact and fast-moving event while Hurricane Isabel exhibited high intensity and prolonged rainfall (Beven and Cobb, 2003; Lixion and Cangialosi, 2011). These distinctive characteristics strongly influence NIs, thereby requiring a generalized approach to define hurricane stages that are consistent across different events. To characterize NIs, we define a landfall stage based on the transition of Net_NI at the coast (e.g., difference between S5 and S1) from dampening to amplification phase within the hurricane event, i.e., negative to positive Net_NI magnitude. The end of the landfall stage is marked by the reverse transition from amplification to dampening phase. The rationale of this definition lies in the assumption that hurricanes primarily enhance positive interactions among the drivers of NIs, leading to a surge in water levels and intensified system responses. The pre- and post-landfall stages are each defined as half the duration of the landfall stage. Each stage of the

hurricane—pre-landfall, landfall, and post-landfall—is indicated by background shading in purple, orange, and teal, respectively, in Figs. 3, 10. This proportional approach ensures that the pre- and post-landfall stages are dynamically scaled to each event, reflecting the system's gradual transition into and out of extreme force.

4. Results and discussion

To efficiently characterize both the annual and tropical cyclone-induced NIs, we will analyze time-series from three representative stations located in the lower, middle, and upper side of the Chesapeake Bay (Fig. 1b) as well as spatial maps of pre-landfall, landfall, and post-landfall hurricane stages. The representative stations are Kiptopeke (KK) located at the eastern shore of Virginia (NOAA: 8632200), Lewisetta (LEW) located at the confluence of the bay with the Potomac River (NOAA: 8635750), and Annapolis (ANN) located at the western shore of the bay (NOAA: 8575512). Model simulations of NIs in the Chesapeake Bay exhibit substantial variability throughout the year as they are driven by a combination of synoptic-scale atmospheric disturbances, including cold fronts, tropical and extratropical cyclones, and seasonal variations in wind forcing. This leads to highly distinct annual NIs patterns characterized by irregular oscillations (Fig. 3). Note that the temporal signature of high-energy hurricane events is considerably different from the annual fluctuations observed during non-extreme events (Fig. 3a-f. Therefore, the subsequent analyses focus first on characterizing the combined effects of tide–driver interactions and their associated NIs during tropical cyclones, and on understanding how these differ from the annual (non-extreme) NIs observed under normal conditions.

4.1. Spatiotemporal dynamics of driver interactions and NIs

To better understand how the combined effects of individual drivers and their respective NIs evolve across different phases of hurricane impact, Fig. 3 illustrates the temporal progression at coastal (KK) and

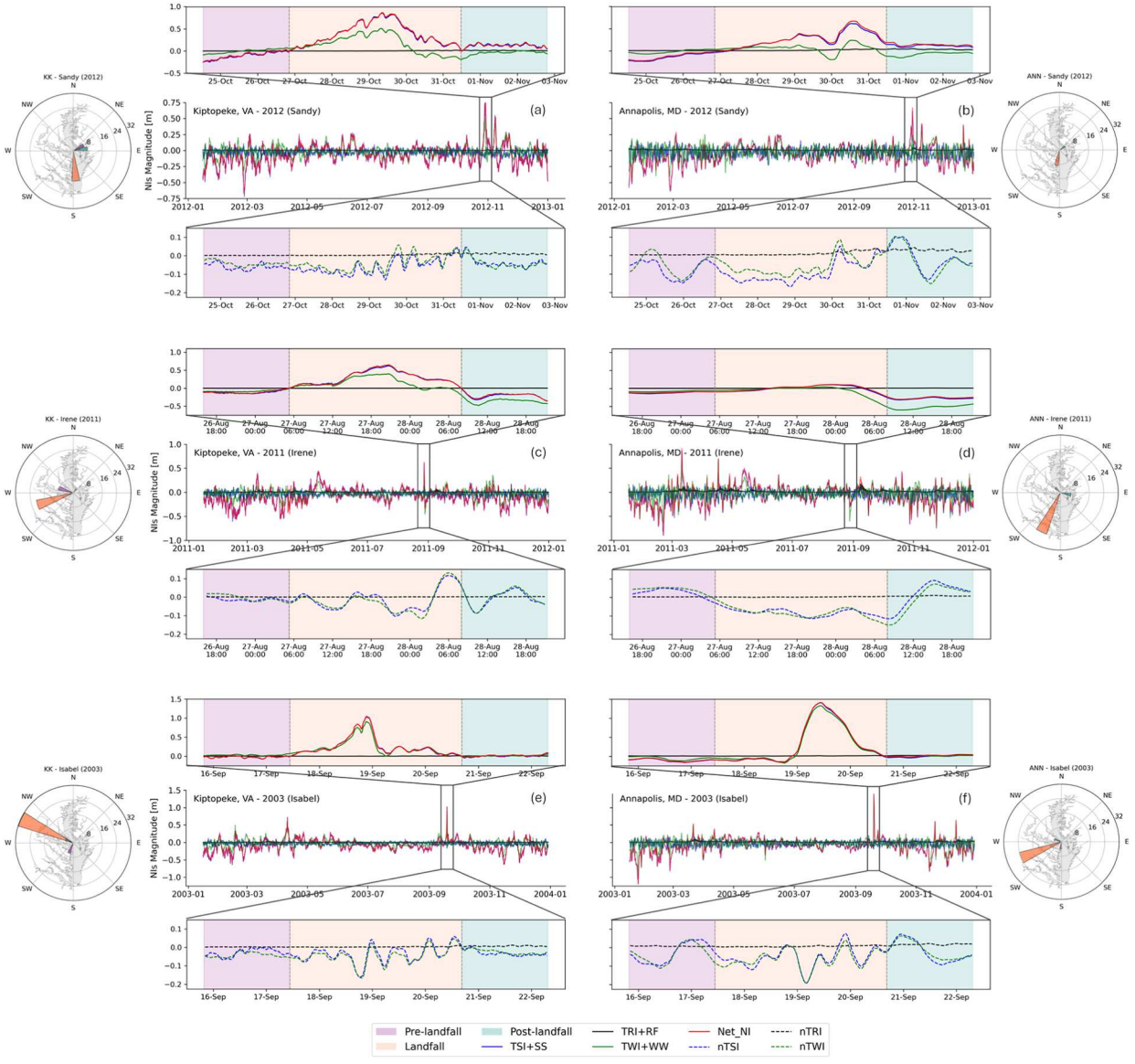

Fig. 3. NIs along with tropical cyclone-induced fluctuations at coastal (left panel) and inland (right panel) stations. Panels (a), (c), and (e) show results at KK station for the years 2012 (Sandy), 2011 (Irene), and 2003 (Isabel), respectively. Panels (b), (d), and (f) show results at the Annapolis station for the same years. The upper zoomed-in insets highlight the combined effects of each driver and its nonlinear interaction (TSI+SS, TRI+RF, and TWI+WW), while the lower zoomed-in insets show only the nonlinear interactions (nTSI, nTRI, and nTWI) during the hurricane events. Purple, orange, and light-green background indicates hurricane's pre-landfall, landfall, and post-landfall stages, respectively. The wind rose plots represent 3-hour averaged wind field (m/s) corresponding to the absolute maximum Net_NI timestamp at the coast for the hurricane stages. Results of mid-bay Leweitte (LEW) station are shown in supplementary material Figure S6.

inland (ANN) stations during three major hurricanes—Sandy (2012), Irene (2011), and Isabel (2003). The upper zoomed-in insets in Fig. 3 highlight the combined effects of each driver and its associated nonlinear interaction (TSI+SS, TRI+RF, and TWI+WW), while the lower insets isolate the nonlinear interaction components alone (nTSI, nTRI, and nTWI) during the hurricane events. The background shading—purple, orange, and teal—indicates the pre-landfall, landfall, and post-landfall stages, respectively. In the pre-landfall stage, the Net_NI predominantly exerts a dampening effect on the system leading to lower TWLs relative to the predicted astronomical tide. As the hurricane makes landfall, the Net_NI reaches a peak amplification, reflecting intensified NIs driven by storm dynamics. However, in the post-landfall stage, the Net_NI decreases either stabilizing at a lower positive magnitude (residual) or transitioning into a dampening phase as the system gradually reverts to normal conditions.

The upper zoomed-in insets in Fig. 3 show that nonlinear interactions (e.g., nTSI, nTWI) intensify during hurricane landfall compared to annual conditions fluctuations. Pre-landfall responses are largely dampening downstream, while upstream signals vary by event. Overall, nTSI and nTWI exhibit similar amplification–dampening patterns, with nTSI showing stronger dampening and nTRI largely negligible. While coupled effects like TSI+SS or TWI+WW display distinct peaks, their nonlinear components do not. Near the coast (KK: Fig. 3a, c, e), NI fluctuates irregularly at high frequency, whereas upstream (ANN: Fig. 3b, d, f), the fluctuations are slower and more persistent, with less abrupt shifts between amplification and dampening effect on the system. This contrast reflects the influence of local dynamics. Near the coast, the system responds rapidly to external forcing, while upstream, increased friction and tidal attenuation dampen and delay the response, resulting in more gradual and sustained nonlinear variations.

4.1.1. *Tide-Surge and tide-wind wave interactions*

Among the three combined tide-driver contributions (interaction + diver effect), TSI+SS has the highest magnitude followed by TWI+WW. TSI+SS is nearly identical to Net_NI in terms of magnitude as well as amplification to dampening phase behavior. Furthermore, TWI+WW maintains a similar progression across the hurricane stages despite its relatively lower magnitude. Differences between TWI+WV and Net_NI are more noticeable in hurricanes with lower sustained wind speeds like those in Sandy (129 km/h) whereas the difference is minimal for higher sustained winds like those in Isabel (160 km/h). Fig. 3 shows that nTSI and nTWI predominantly act as dampening influences on the system, especially during the pre-landfall and post-landfall stages. However, during landfall, both occasionally exhibit positive peaks, indicating short-lived amplification. Overall, nTSI exhibits a more consistent and stronger dampening effect than nTWI during slow-moving systems like Hurricane Sandy (Fig. 3a-b), due to prolonged tide–surge interactions. In contrast, for faster-moving storms such as Hurricane Irene (Fig. 3c-d), nTWI appears more prominent, while the nTSI signal dissipates more quickly, suggesting that storm translational speed influences which nonlinear mechanisms dominate. At the upstream station in Annapolis during Hurricane Irene (Fig. 3d), although the combined effects of TSI+SS and TWI+WW remain close to zero (leading from pre-landfall through landfall stage) their NI remains very strong, fluctuating between +0.05 m and –0.15 m. This highlights that a weak or neutral combined tide–driver interaction effect does not imply a negligible nonlinear response. Rather, NIs are fundamentally non-additive, they can intensify due to internal feedback, phase mismatches, or resonant amplification, even when the effect of external forcing appears minimal. As such, the behavior of combined tide–driver effect and their associated nonlinear response are not always directly correlated, underscoring the importance of explicitly isolating NIs when interpreting system dynamics during extreme events.

4.1.1.1. Pre-landfall stage. In general, the Chesapeake Bay exhibits a dampened phase represented in the negative TSI+SS (Fig. 4a-c) and TWI+WV (Fig. 6a-c). For Hurricane Sandy, the dampening effect is relatively stronger compared to the other two hurricanes. The wind field vectors in Figs. 4a and 6a indicate that Sandy had a relatively weak pre-landfall wind speed of 2.79 m/s, originating from the southwest. According to the NOAA meteorological data, the Chesapeake Bay experienced consistently elevated atmospheric pressure throughout the pre-landfall stage, averaging approximately 1020.5 mb at SP station and leading to a negative pressure-driven surge. In fact, observed data shows that this high-pressure ridge off the U.S. East Coast created an enhanced barometric gradient that caused a stronger outward flow of water from the system.

However, in the case of fast-moving hurricanes like Irene, the offshore wind fields were relatively strong, averaging around 6.82 m/s over the Chesapeake Bay. Here, the negative TWI remained dominant, indicating that wind-driven offshore transport outweighed the effects of elevated pressure (1015.3 mb at SP station). The spatial distribution of TSI+SS indicates a stronger dampening effect for Hurricane Irene along the Atlantic coast, which gradually attenuated westward into its middle bay tributaries (Fig. 4b). In contrast, the negative TSI+SS interaction for Hurricane Isabel is greater in the upper bay indicating a gradual outflow toward the coast (Fig. 4c). Both of these spatial distributions align with the wind directions observed during their respective pre-landfall stages. However, Hurricane Sandy shows a different pattern where the dampening effect is considerably stronger near the coast due to a negative pressure-driven surge. Also, the system experiences weak cross-bay wind towards the northeast (Fig. 4a).

When isolating the nonlinear components, Figs. 5a and 7a show that Hurricane Sandy's nTSI and nTWI exhibits strong negative values across the mid and upper Chesapeake Bay, reaching up to –0.12 m. This NI intensifies the negative drawdown surge during the pre-landfall phase. While the total interaction fields (TSI+SS, TWI+WW) for Sandy displays a down-Bay intensification in magnitude their nonlinear components do not follow this gradual pattern. Instead, nTSI and nTWI have the strongest dampening response mid to upper bay region. This suggests that nonlinear processes exert a spatially distinct influence compared to the total tide-drive interaction response. During the pre-landfall stage of all three hurricanes (Figs. 4a-c, 6a-c), the lower Chesapeake Bay consistently exhibits a strong dampening effect in both TSI+SS and TWI+WW. In this region, their nonlinear components (nTSI, nTWI) are generally in phase with the driver-induced response, reinforcing offshore-directed transport. In contrast, the mid and upper Bay shows positive NI zones for Hurricane Irene and Isabel. Here, nonlinear effects act as compensatory mechanisms counteracting surge and wind-wave induced forcings. This behavior may be tied to how long the storm system influences the Bay during its pre-landfall approach. For the slow-moving hurricanes (e.g., Sandy), the nonlinear components act in synergy with the driver-induced response in the pre-landfall phase. Meanwhile, the relatively faster-moving storms (e.g., Irene, Isabel)—exhibit stronger compensatory nonlinear effects in the mid and upper Bay. This suggests that faster-moving storms, due to their shorter residence time and more transient forcing are more likely to induce phase mismatches among tides, surge, and wind-driven waves, resulting in destructive interference that reduces the system's overall extreme response.

4.1.1.2. Landfall stage. During landfall, each of the hurricanes exhibits a positive amplification of the tide-driver interaction response. This, in turn, produces an elevated surge level near the coast that is driven by the combined effect of wind forcing, atmospheric pressure, and tides. As a result, TSI+SS closely aligns with Net_NI suggesting that pressure and wind are the dominant drivers in this stage (Fig. 4d-f). However, there is a considerable gap between TSI+SS and TWI+WW for Hurricane Sandy at both the KK and the ANN stations indicating a strong influence of pressure-driven surge in the Chesapeake Bay (Figs. 4d and 6d). This is largely influenced by the slower movement of the hurricane, which

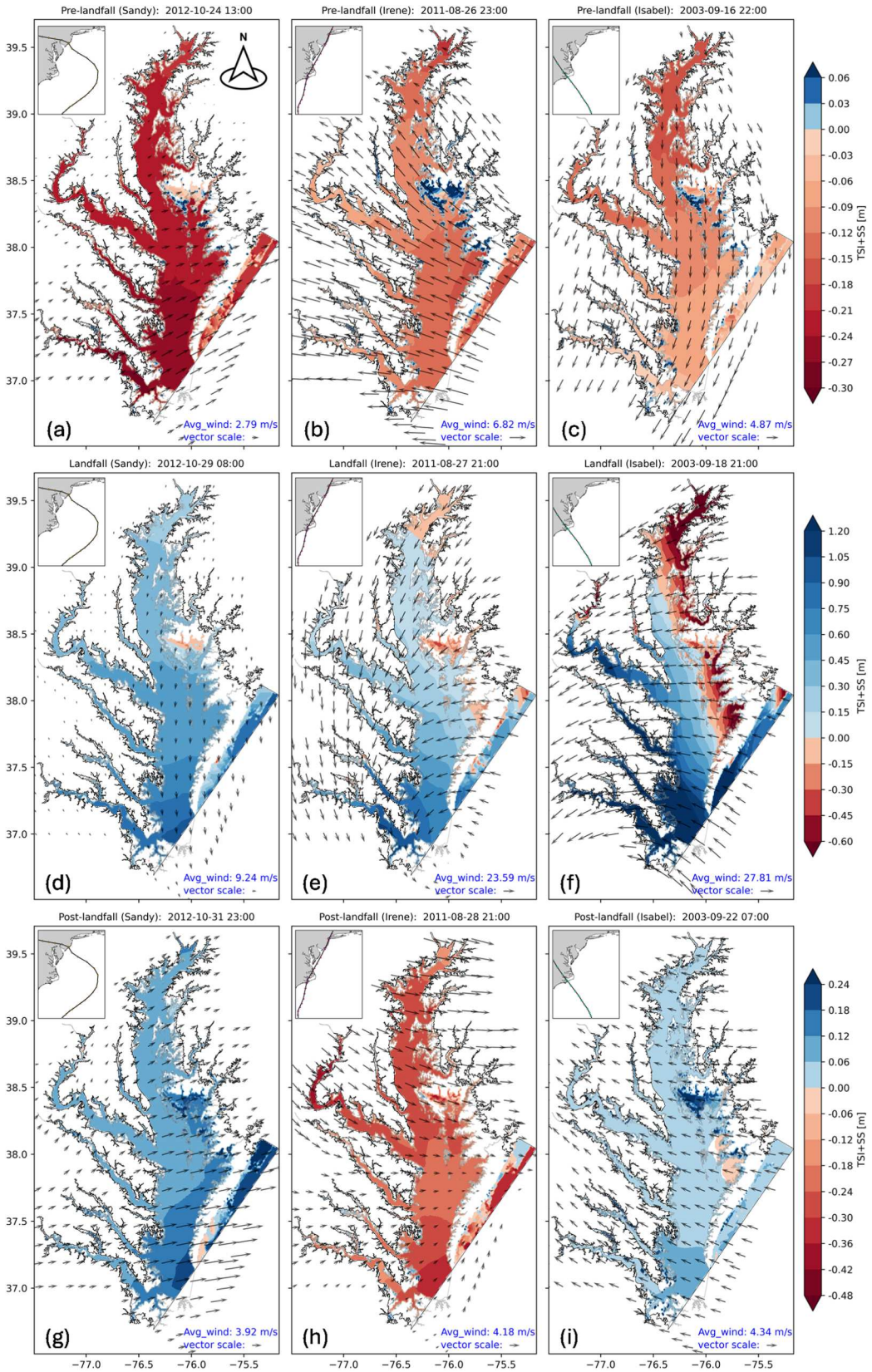

Fig. 4. Spatial distribution of the combined effect of TSI+SS across the Chesapeake Bay. The timestamp coincides with the absolute maximum Net_NI at KK station for each hurricane and stage. Horizontal panels represent (a-c) pre-landfall, (d-f) landfall, and (g-i) post-landfall stages whereas vertical panels indicate the three hurricanes. Negative and positive magnitudes indicate dampening and amplification phases in the system, respectively. Wind vectors represent the average wind speed at the timestamp.

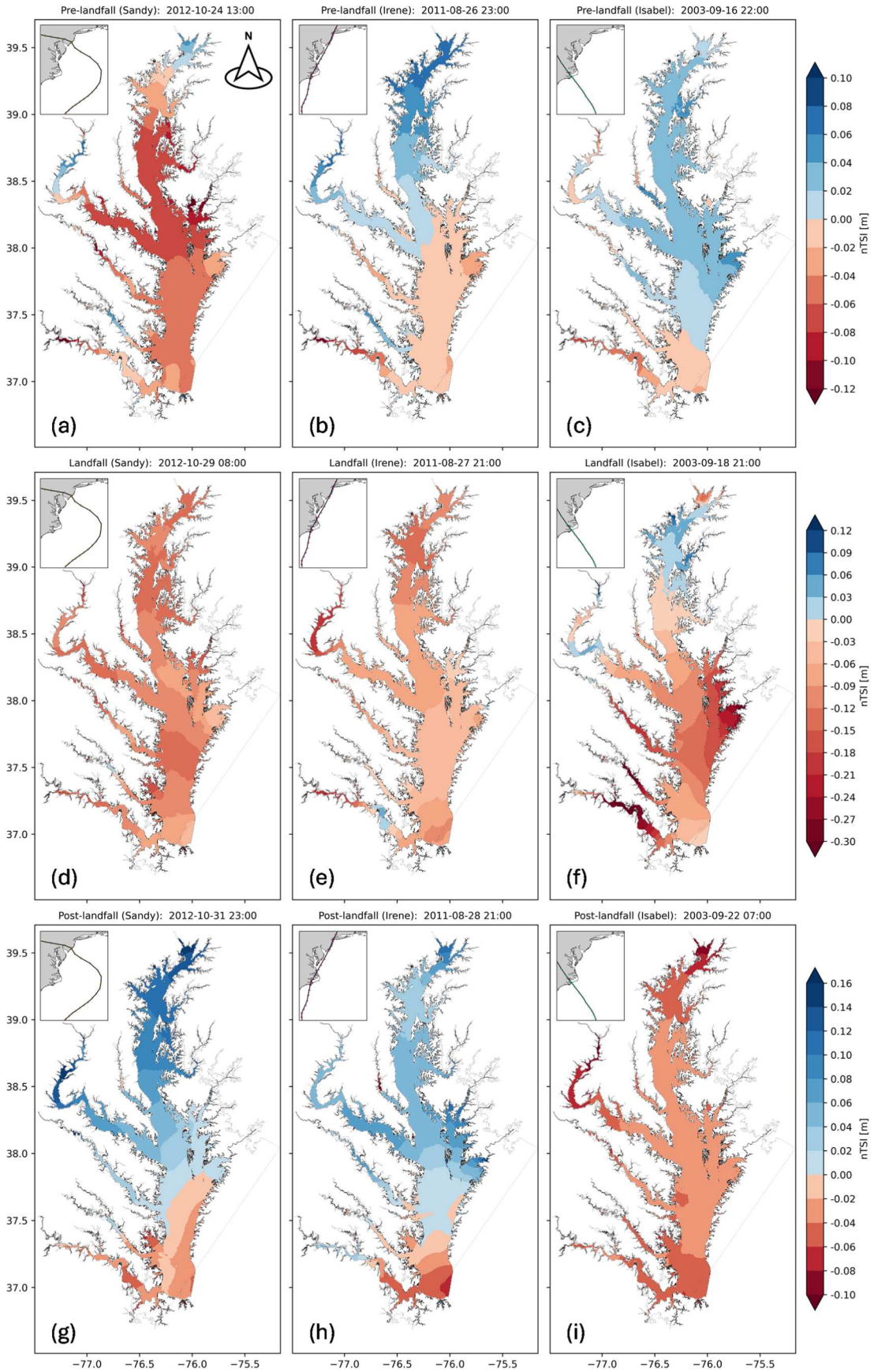

Fig. 5. Spatial distribution of nTSI across the Chesapeake Bay. The timestamp coincides with the absolute maximum Net_NI at KK for each hurricane and stage. Horizontal panels represent (a-c) pre-landfall, (d-f) landfall, and (g-i) post-landfall stages whereas vertical panels indicate the three hurricanes. Negative and positive magnitudes indicate dampening and amplification phases in the system, respectively.

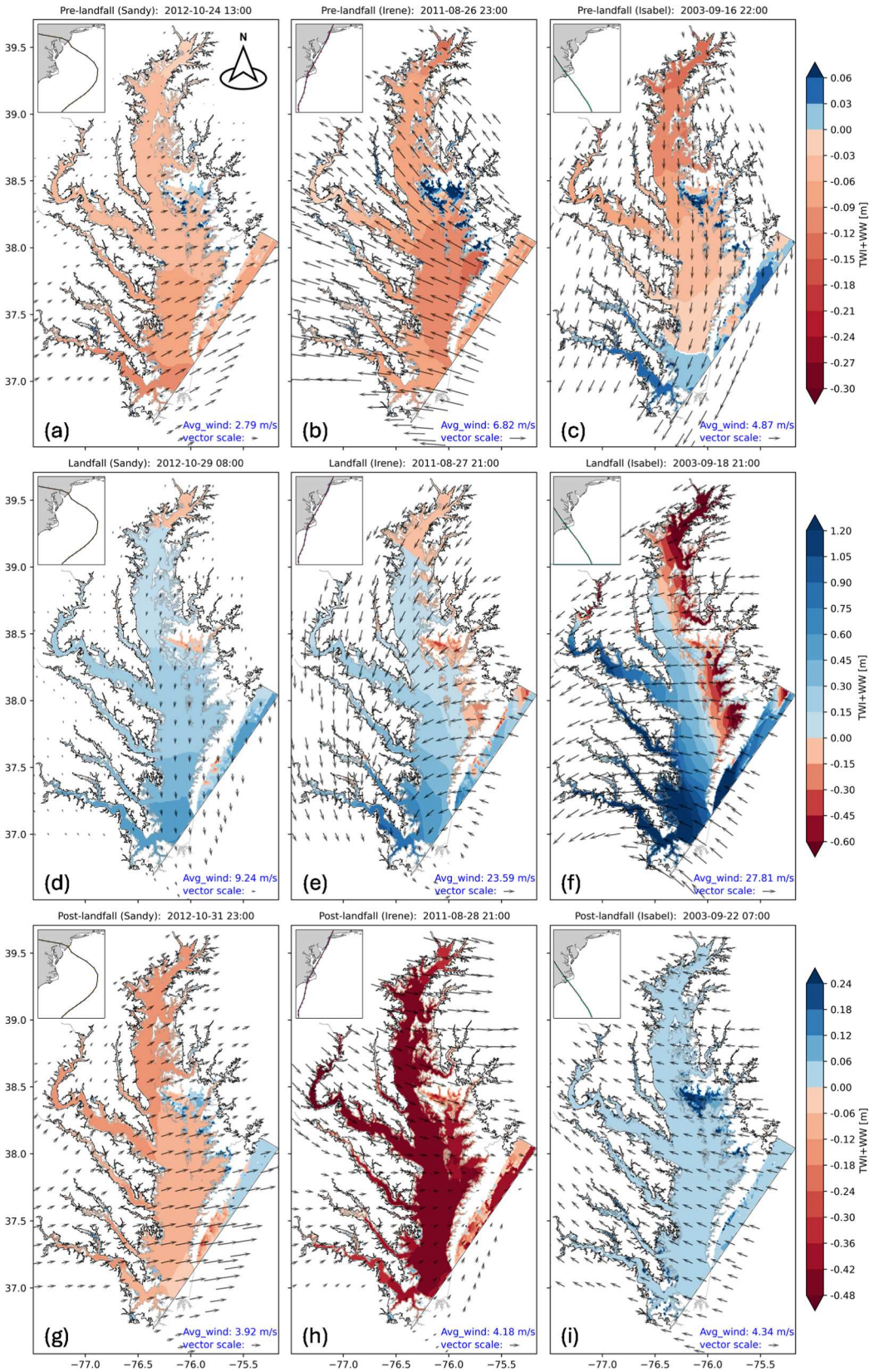

Fig. 6. Spatial distribution of the combined effect of TWI+WW across the Chesapeake Bay. The timestamp coincides with the absolute maximum Net_NI at KK for each hurricane and stage. Horizontal panels represent (a-c) pre-landfall, (d-f) landfall, and (g-i) post-landfall stages whereas vertical panels indicate the three hurricanes. Negative and positive magnitudes indicate dampening and amplification phases in the system, respectively. Wind vectors represent the average wind speed at the timestamp.

allows the inverse barometer effect to exert a greater impact as the system has more time to respond to a sustained low pressure. Consequently, while TWI+WW is still dominant, the pressure-driven surge remains a key factor in determining the system response in slow-moving low-pressure systems. In contrast, the wind field of faster-moving hurricanes like that of Isabel allows less time for pressure-induced surge to develop. As a result, wind stress became the primary driver with TWI+WW dominating the net system response. The gap between TSI+SS, TWI+WW is therefore minimal at the peak surge (Figs. 4f and 6f). This suggests that wind setup dominates over the inverse barometer effect for hurricane events with very strong wind fields and faster translational speed.

The spatial patterns of TSI+SS and TWI+WW are also influenced by the hurricanes' trajectory, wind field patterns, and direction. Hurricane Sandy approached the U.S. Atlantic Coast from the southeast and made landfall near Atlantic City, New Jersey (Fig. 1a). This path positioned the Chesapeake Bay to the south of the storm center. Due to its counterclockwise wind circulation, regions to the south of the storm's eye experience winds primarily from the northwest. This wind pattern pushed water toward the eastern coast (KK), amplifying its Net_NI while reducing it along the western shoreline (LEW and ANN). Therefore, tide-driver interaction effect is more pronounced near the coast where wind effects are more direct leading to stronger TSI+SS and TWI+WW in coastal areas (Figs. 4d and 6d). Hurricane Irene moved northward parallel to the Chesapeake Bay but stayed to the east of the bay (Fig. 1a). Due to its counterclockwise rotation, its onshore winds created an initial surge near the coast that continued propagating towards the middle bay. Its southwest wind trajectory enhances wind-driven water transport. Therefore, TSI+SS and TWI+WW interact strongly at western coast to the middle bay (Figs. 4e and 6e). However, this strong wind force results in a mild drawdown effect in the upper bay and eastern tributaries. This leads to negative TSI+SS and TWI+WW responses at the peak surge. In contrast, Hurricane Isabel followed a northwestward path and made landfall on the Outer Banks of North Carolina before moving inland west of the Chesapeake Bay (Fig. 1a). Initially, its expansive wind field generated strong southerly winds, funneling water northward into the bay. After landfall, its inland trajectory generated strong westerly winds at the peak surge. This strong cross-bay wind field led to sustained high TSI+SS and TWI+WW response in the lower to middle bay (Figs. 4f and 6f). Note that for large coastal systems like the Chesapeake Bay, TSI+SS, TWI+WW at the landfall stage does not exclusively lead to positive magnitude or amplification phase. Instead, depending on the wind speed and direction, these interactions can induce substantial dampening effects. When wind forces are strong enough, they can laterally redistribute water across the bay and effectively override pressure-driven surge; thus, influencing the expected water level rise associated with atmospheric pressure drop. This underscores the critical role of wind forcing, not only in surge magnitude but also in shaping the complex asymmetry of TSI+SS and TWI+WW response in the system.

In the landfall phase, the dominance of tide-surge interactions is apparent, with TSI+SS consistently exhibiting stronger amplification or dampening to TWI+WW in total system response. This behavior carried through to their nonlinear counterparts (Figs. 5d-f and 7d-f) shows that nTSI has a stronger dampening response than nTWI mirroring the stronger modulation observed in surge–tide dynamics. While TSI+SS and TWI+WW are predominantly positive across the Bay, their nonlinear components (nTSI, nTWI) generally act in an opposing manner, directly countering the driver-induced response. This compensatory pattern persists even in negative TSI+SS and TWI+WW phases. For example, during Irene, the far upstream region shows strong negative TSI+SS and TWI+WW values, yet the corresponding nonlinear component in those areas shows positive amplification, reaching up to +0.10 m. This reflects a recurring out-of-phase behavior between NI and its corresponding tide–driver interaction. However, this pattern breaks down along the western mid-Bay shoreline during Isabel landfall (Figs. 5f and 7f). Here, the negative nonlinear interaction (nTSI, nTWI ≈ –0.30 m) reinforces the dampening induced by TSI+SS, TWI+WW, directly contributing to the seiching effect. This implies that NI are not uniformly compensatory, rather under certain hurricane conditions (e.g., intensity, translational speed, wind direction, landfall angle) they can amplify system asymmetries and enhance localized system response.

4.1.1.3. Post-landfall stage. At the onset of the post-landfall stage, Hurricane Irene's offshore winds were relatively strong and well-channeled towards the southeast direction. This accelerated the removal of the residual surge, offsetting the still-positive inverse barometric effect caused by the low-pressure system. Consequently, in the later post-landfall stage, the system exhibits a negative TSI+SS and TWI+WW response (Figs. 4h and 6h). In contrast, Hurricane Sandy exhibited a weaker and more diffuse post-landfall wind pattern, predominantly towards the eastern shoreline. While offshore winds were still present, they were not as strong as Hurricane Irene. This resulted in a negative TWI+WW (Fig. 6*g*), but with a weak drawdown effect. In fact, Hurricane Sandy's slower dissipation rate and broader wind field allowed residual surge to persist, which in turn sustained a net positive TSI+SS throughout the post-hurricane stage (Fig. 4*g*). In the case of Hurricane Isabel, the Net_NI magnitude fluctuates close to zero (Fig. 3e-f, Figure S6c). Their spatial distributions show minimal TSI+SS (Fig. 4i) and TWI+WW (Fig. 6i) positive response due to the onshore northwesterly winds flowing into the Chesapeake Bay system.

These variations in the total response extend to their nonlinear components. In Hurricane Sandy, both nTSI (Fig. 5*g*) and nTWI (Fig. 7*g*) exhibit strong positive values in the upper and mid-Bay, with nTWI reaching up to +0.15 m. This nonlinear amplification reflects the sustained influence of Sandy's residual surge, particularly in northern Bay. As for Hurricane Irene, while TSI+SS and TWI+WW exhibit strong negative responses (driven by strong offshore winds), both nTSI (Fig. 5h) and nTWI (Fig. 7h) show positive amplification in the mid-to-upper Bay region. This out-of-phase behavior suggests that even as the dominant wind and surge effects subside, NIs actively contribute to maintaining elevated water levels. In contrast, Hurricane Isabel's NI displays a reversed yet still compensatory dynamic. While TSI+SS and TWI+WW show broad post-landfall amplification, the corresponding nonlinear components are consistently negative, with dampening strongest in the upper Bay and western tributaries. As with Irene, this reflects a compensatory nonlinear response, but in Isabel's case it actively offsets elevated water levels rather than supporting them. Together, these cases reinforce the recurring pattern in which NI acts out of phase to either sustain or accelerate drawdown depending on the storm's wind direction, intensity, and inland trajectory.

4.1.2. Tide-River interactions

TRI+RF magnitude is negligible compared to TSI+SS and TWI+WV across the Chesapeake Bay and exhibit a rather constant spatiotemporal pattern. In fact, the combined effect of TRI+RF and nTRI is negligible with only minor millimeter-scale variations across the pre-landfall, landfall, and post-landfall stages (Fig. 3). The upper zoomed-in insets in Fig. 3c-d show that nTRI is virtually absent during Hurricane Irene. However, minor post-landfall fluctuations on the order of a few millimeters (<3 mm) are observed at the coastal station (KK: Fig. 3a, e) during Hurricanes Sandy and Isabel. These nTRI fluctuations are more pronounced at the upstream station (ANN: Fig. 3b, f) due to the enhanced sensitivity of river–tide interactions farther inland. Fig. 8 shows the spatial distribution of TRI+RF is also negligible across the system, with little to no amplification or dampening. While previous studies e.g., (Cai et al., 2019; Kästner et al., 2019; Sassi and Hoitink, 2013) have shown that tide–river interactions can alter water level response in tidal river systems, our analysis of TRI + RF and nTRI reveals that the magnitude of nonlinear interactions exhibits a weak spatiotemporal signal, largely dependent on the magnitude and timing of riverine inflow during preceding hurricane stages. This is most

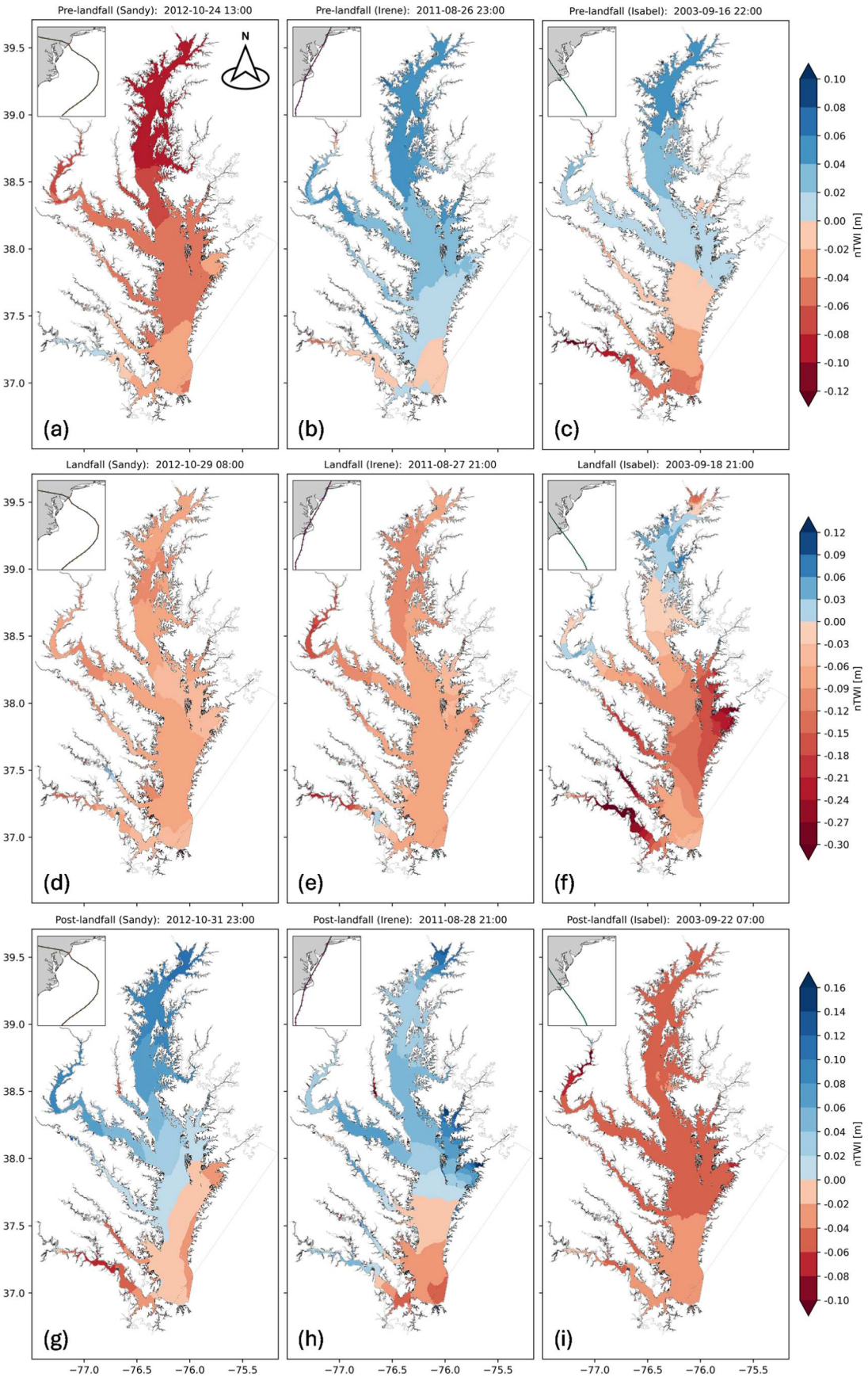

Fig. 7. Spatial distribution of nTWI across the Chesapeake Bay. The timestamp coincides with the absolute maximum Net_NI at KK for each hurricane and stage. Horizontal panels represent (a-c) pre-landfall, (d-f) landfall, and (g-i) post-landfall stages whereas vertical panels indicate the three hurricanes. Negative and positive magnitudes indicate dampening and amplification phases in the system, respectively.

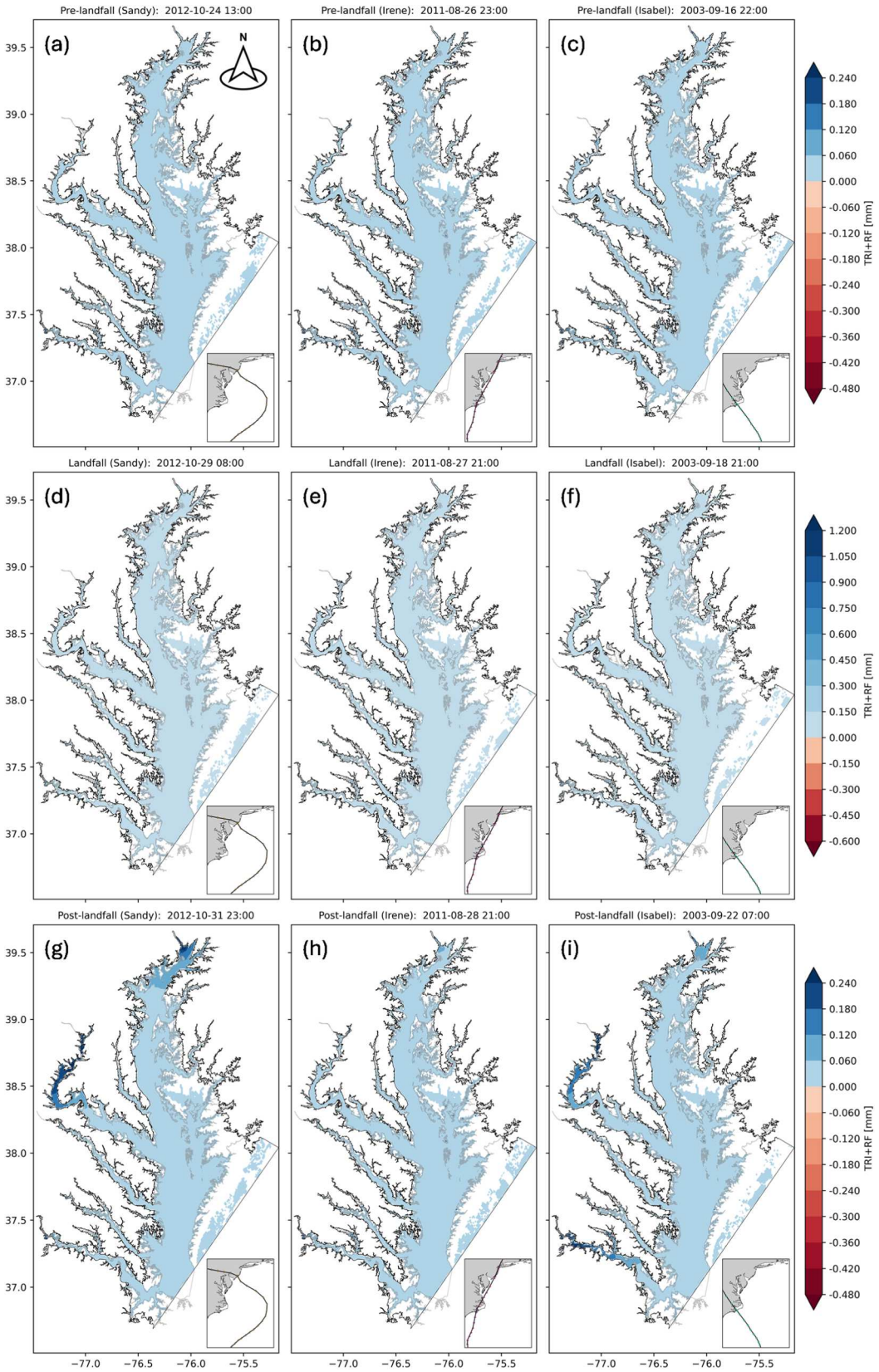

Fig. 8. Spatial distribution of the combined effect of TRI+RF across the Chesapeake Bay. The timestamp coincides with the absolute maximum Net_NI at KK for each hurricane and stage. Horizontal panels represent (a-c) pre-landfall, (d-f) landfall, and (g-i) post-landfall stages whereas vertical panels indicate the three hurricanes. Negative and positive magnitudes indicate dampening and amplification phases in the system, respectively. Wind vectors represent the average wind speed at the timestamp.

noticeable as positive TRI + RF and nTRI magnitudes during the post-landfall stage in the upper bay, particularly near the Susquehanna River and along major tributaries such as the Potomac and James Rivers.

TRI+RF and nTRI is primarily driven by upstream river flow where high freshwater discharge interacts with tides by enhancing frictional effects due to hydraulic drag; thereby, increasing mean water level and decreasing the tidal range (Ralston et al., 2019; Sassi and Hoitink, 2013). As a result, no noticeable river–tide nonlinearities (Fig. 9a-f) are observed during the pre- and landfall stages due to moderate to low upstream river flow. However, post-landfall spatial distribution shows a strong TRI + RF (Fig. 8*g*) and nTRI (Fig. 9*g*) signal originating from the Potomac River corridor for Hurricane Sandy. In particular, the USGS gauge recorded a net cumulative discharge of 9500 m^3/s during the hurricane stages. Similarly, the upstream bay below the Susquehanna River boundary exhibits a high TRI + RF and nTRI magnitude, resulting from a total of 15,000 m^3/s discharge during the event. In contrast, Hurricane Irene did not generate substantial hurricane-induced rainfall-runoff, resulting in negligible TRI + RF (Fig. 8f) and nTRI (Fig. 9f) magnitude across the three phases of the hurricane event. For Hurricane Isabel positive values are observed downstream of the Potomac and James Rivers which can be explained by the relatively high cumulative discharge of 10,200 m^3/s and 6500 m^3/s, respectively (Fig. 8i). Nevertheless, TRI+RF and nTRI fluctuations near the coast are negligible as tidal energy dominates in the lower estuary, while riverine influence is more localized and stronger in the upper bay.

4.2. Annual vs. hurricane-induced variability in driver interactions and NIs

The simulations of annual NIs exhibit positive and negative magnitudes that are driven by various meteorological and oceanographic processes, including tropical (hurricanes) and extratropical cyclones (Nor'easters), frontal systems, and large-scale atmospheric pressure shifts (Fig. 3). To separate annual non-extreme NIs from those induced by tropical cyclones or other extreme anomalies, we set a threshold value of two standard deviations (±2σ) around the mean Net_NI (e.g., [−0.212 m, 0.344 m]). Positive or negative magnitudes within this range (Supplementary Figure S7) are considered annual NIs driven by offshore-onshore wind patterns, seasonal variations, and associated pressure fluctuations.

To understand the distributional shift in NIs magnitude and variability across different hurricane landfall stages, Kernel Density Estimation (KDE) plots are presented in Fig. 10. KDE is a non-parametric way to estimate the probability density function of a dataset, making it particularly useful for identifying the underlying distribution and central tendencies of complex, non-uniform data (Węglarczyk, 2018). Since the annual NIs dataset is substantially larger compared to the hurricane event dataset, the resulting scale discrepancy makes direct visual comparisons of KDE plots ineffective. Specifically, the annual dataset consists of 1031 days calculated by considering three years of simulation, removing the first 15 days of data from each year, and excluding the corresponding duration of the three hurricane events. Within this dataset, 94.5 % of the data falls within the ±2σ threshold that is equivalent to 975 days. Given that each hurricane event lasts for an average of 6.67 days, the baseline dataset is approximately 150 times larger than the duration of an average hurricane event. The difference in dataset size alters the density scale, causing the baseline KDE to appear disproportionately taller and narrower compared to the wider and shorter KDE plots of the hurricane events. Therefore, to address this issue and ensure comparability, a Monte Carlo sampling approach was applied by resampling the annual NIs dataset 500 times and creating an ensemble (Fig. 10, gray lines). This approach ensures that annual variability is preserved, while also allowing the KDE plots for the baseline and different hurricane stages to remain visually comparable on the same scale.

The normal distribution of the resulting ensembles suggests that the annual response of combined tide–driver interactions and their associated NIs fluctuates symmetrically around a zero-state. Also, note that KDEs exhibit a high degree of normality with mean values of −0.05 m for TSI+SS, 0.01 m for TRI+RF, and −0.01 m for TWI+WW averaged across the three stations. The negative TSI+SS and TWI+WW indicate that these drivers impose an overall dampening effect on the Chesapeake Bay. Furthermore, these serve as the reference for evaluating the evolution of tropical cyclone-induced tide-driver interaction and its NIs during pre-landfall, landfall, and post-landfall stages. The baseline ensemble (gray lines) shows that the annual distributions of nTSI and nTWI are approximately normal, with a slight negative peak around –0.025 m, reflecting a weak but consistent dampening influence under non-extreme conditions. In contrast, nTRI displays a strong positive skew similar to its parent component TRI+RF suggesting that tide–river nonlinear interactions more frequently amplify water levels. Notably, the annual fluctuation range of nTSI and nTWI is broader at the upstream ANN station (Fig. 10j, p: –0.25 m to +0.15 m) than at the coast KK (Fig. 10l, r: –0.15 m to +0.08 m), indicating greater variability inland. In general, the KDE plots of TSI+SS, TRI+RF, TWI+WW, nTSI, nTRI and nTWI show a consistent shift toward higher magnitudes during landfall across all hurricanes (Fig. 10), regardless of the hurricane's best track that was parallel to the coast (Irene), right side (Sandy), or left side (Isabel) of the Chesapeake Bay (Fig. 1a).

4.2.1. Pre-landfall stage

During the pre-landfall stage, the KDE plots of TSI+SS (Fig. 10a-c) and TWI+WW (Fig. 10g-i) are primarily skewed toward negative values, indicating an early-stage dampening effect driven by positive pressure anomalies and offshore winds that begin to alter NIs. In contrast, the KDE plot of TRI+RF is aligned with that of the annual NIs (Fig. 10d-f). The dampening effect of TSI+SS and TWI+WW is particularly strong for the relatively fast-moving hurricanes Irene and Isabel, both of which exhibit a sharp negative spike in the pre-landfall stage. Stations located in the lower bay (KK) show minimal shifts of the KDE plot with respect to that of the annual NIs, while stations located in middle and upper bay (LEW, ANN) show a stronger dampening effect. This suggests that combined tide-driver interaction effect in the pre-landfall stage is location-dependent and possibly linked to basin-scale wind setup or early baroclinic water level adjustments. A similar pattern emerges in the nonlinear components in the pre-landfall stage. The nTSI and nTWI distributions (Fig. 10j-l, p-r) are also skewed negatively, particularly at mid- and upper-bay stations, indicating that the early-stage dampening observed in the combined effects is partially driven by underlying nonlinear interactions. Notably, in the upstream region (ANN), the dampening signal from nTSI and nTWI during Hurricanes Sandy and Isabel exhibits broader distributions with extended negative tails, reflecting a wider spread negative nonlinear response. In contrast, Hurricane Irene shows a distinct positive peak in the mid-bay to upstream region opposite to the dampening behavior seen in TSI+SS and TWI+WW. This divergence highlights the nature of NIs, which can exert an amplifying effect on water levels even when the combined driver effects are enforcing a dampening influence on the system. It also underscores the sensitivity of upstream regions to storm-specific forcing patterns, such as localized wind orientation and pressure setup. In contrast, nTRI remains centered around zero during the pre-landfall stage, suggesting minimal nonlinear tide–river interaction prior to landfall.

4.2.2. Landfall stage

There is a substantial shift of the KDE plots toward higher TSI+SS and TWI+WW magnitudes for all the three stations during landfall regardless of the hurricane's intensity and trajectory. These KDE plots are well-separated from that of the annual NIs, confirming a strong amplification of tide-driver interaction at landfall. Stations located in the lower bay (KK), show a consistent spread and lower inter-hurricane variability in terms of KDE plots for TSI+SS and TWI+WW (Fig. 10a, g).

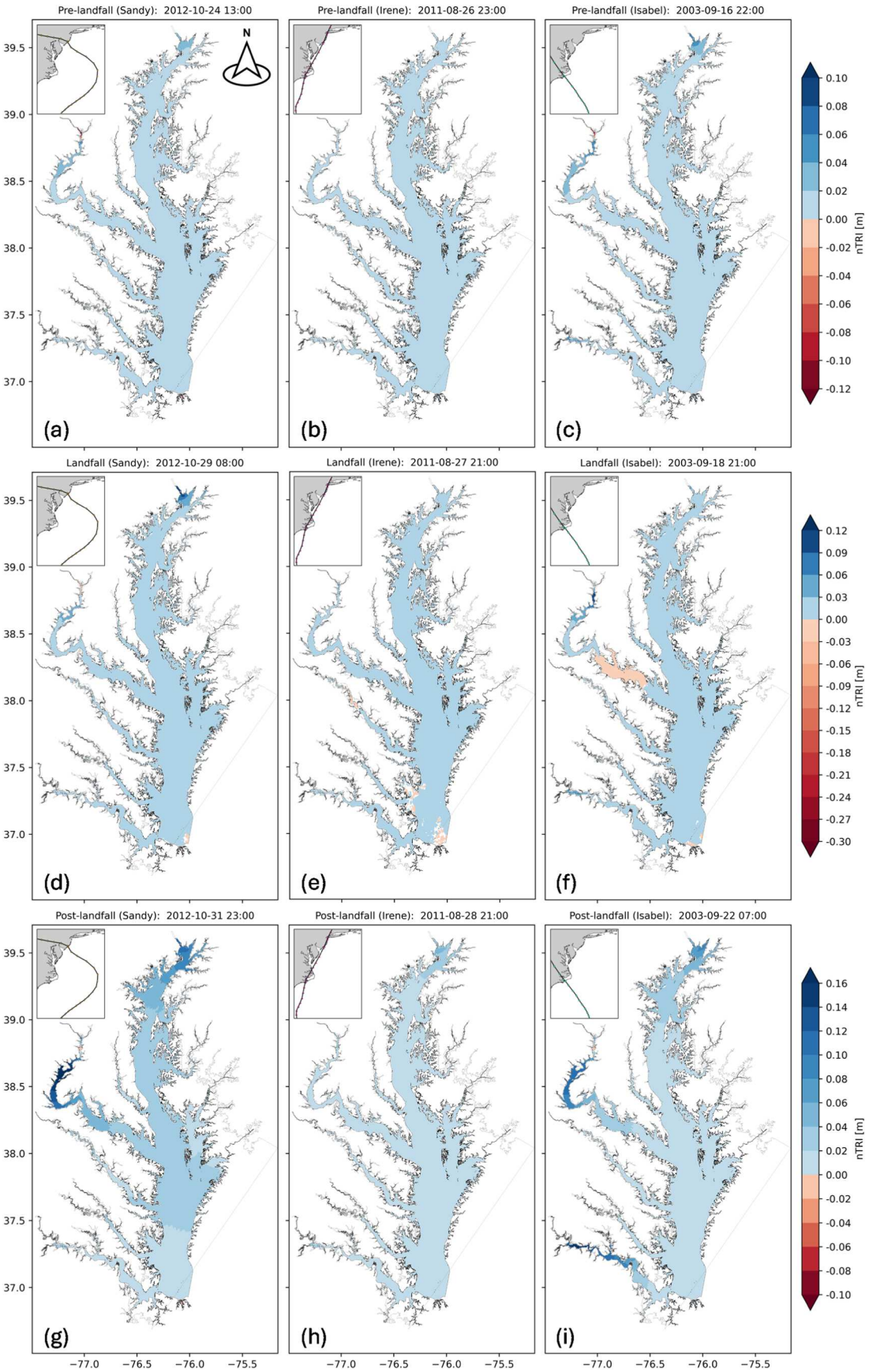

Fig. 9. Spatial distribution of nTRI across the Chesapeake Bay. The timestamp coincides with the absolute maximum Net_NI at KK for each hurricane and stage. Horizontal panels represent (a-c) pre-landfall, (d-f) landfall, and (g-i) post-landfall stages whereas vertical panels indicate the three hurricanes. Negative and positive magnitudes indicate dampening and amplification phases in the system, respectively.

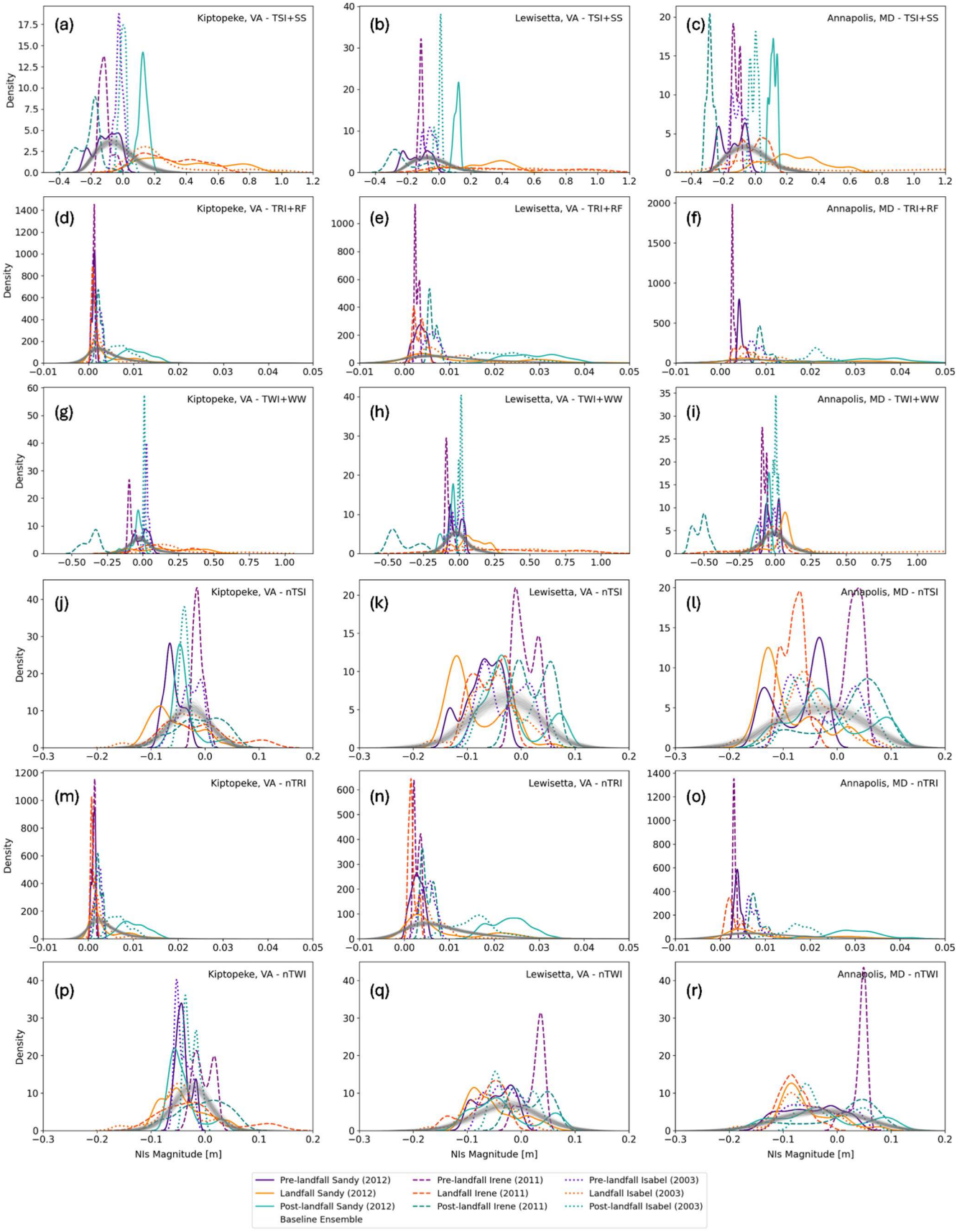

Fig. 10. Kernel Density Estimation of (a-c) TSI+SS, (d-f) TRI+RF, (g-i) TWI+WW, (j-l) nTSI, (m-o) nTRI and (p-r) nTWI for hurricane Sandy (solid line), Irene (dashed line), and Isabel (dotted line). Hurricane stages are color-coded according to the stage: pre- (purple), post- (cyan), and landfall (orange). Lower, middle, and upper bay stations are arranged in vertical panels with Kiptopeke (left), Lewisetta (center), and Annapolis (right). The gray-shaded ensembles represent annual (non-extreme) interactions across the aggregated annual cycle.

However, as we move toward the middle (LEW) and upper bay (ANN), the KDE plots become increasingly dispersed with a greater variance (Fig. 10b, h and c, i). This suggests that TSI+SS, TWI+WW in the middle and upper bay are more sensitive to hurricane characteristics (e.g., wind pattern, direction, pressure drop, track) and local bathymetry as compared to the coast. The KDE plot of TRI+RF exhibits a gradual shift towards positive values particularly in the upper bay due to hurricane-induced rainfall-runoff (Fig. 10f).

Focusing on the NI (Fig. 10j-r) provides further insight into storm response variability. Fig. 10j shows nTSI to have a wide range of interaction values in the lower bay KK (–0.20 m to +0.20 m) indicating a highly dynamic response to storm conditions. However, this signal attenuates considerably in the mid- and upper bay (Fig. 10k-l), where the nonlinear effect becomes predominantly dampening. Particularly, at ANN (Fig. 10l), the landfall-stage nTSI distributions exhibit consistent negative peaks, with density modes around –0.10 m for Irene, slightly below –0.05 m for Isabel, and –0.12 m for Sandy. At the mid-bay station LEW (Fig. 10k), the peak dampening responses are similar for Irene and Isabel (approximately –0.05 m), while Sandy again shows a stronger negative NI response near –0.12 m. Despite this overall dampening trend, the distributions remain relatively broad, indicating localized system response and high sensitivity to storm-specific dynamics even in the upper bay. However, nTWI displays contrasting behavior. At the upstream station ANN (Fig. 10r), the landfall-stage KDEs exhibits very similar distributional pattern across all storms with well-aligned peaks near –0.10 m. At the mid-bay station LEW (Fig. 10q), the distribution begins to spread out, reflecting increased variability across different hurricanes. This variability becomes more pronounced in the lower bay KK (Fig. 10p), where the distributions are broader and exhibit a stronger amplification effect. This suggests that nTWI in the lower bay is more sensitive to hurricane wind fields, whereas the upstream response is more uniform and dampening dominated. Furthermore, unlike nTSI, nTWI maintains a strong presence across all three stations, exhibiting less spatial attenuation and a more consistent influence throughout the estuarian system.

4.2.3. Post-landfall stage

In the post-landfall stage, TSI+SS shift back toward the KDE distribuition of the annual NIs but still exhibit some residual amplifying effects (Fig. 10a-c). For Hurricane Sandy, TSI+SS remains positive across the Chesapeake Bay while that of Irene exhibits a strong dampening effect due to rapid offshore withdrawal. This is a direct response to southwesterly offshore winds that pushed water out of the system and led to a negative TWI+WW response (Fig. 10g-i). While stations in the lower bay experience moderate drawdown due to their connection with the open ocean, the middle and upper bay exhibit progressively stronger negative TWI+WW magnitudes. This suggests that TWI+WW had a more pronounced effect in confined inland areas where water exchange is limited due to restricted hydraulic connectivity with the ocean and weak incoming tides, which reduce the system's ability to offset the wind-induced drawdown. In contrast, the KDE plots of TSI+SS and TWI+WW exhibit very different behavior for Hurricane Irene. While TSI+SS and TWI+WW are not strongly amplified in the upper bay, the overall system response shows considerable variability. This supports the idea that tide-driver interaction response in the post-landfall stage depends on hurricane characteristics. The KDE plot of TRI+RF shows a slight shift towards positive values driven by freshwater discharge in the upper bay (Fig. 10i). This is evident for Hurricane Sandy and Isabel where the total cumulative discharge reached approximately 26,000 m^3/s and 25,600 m^3/s, respectively. In contrast, the KDE plot of TRI+RF shows minimal change due to extremely low runoff of 2175 m^3/s for Hurricane Irene.

In contrast to the spatial variability observed in the combined tide–driver effects, the nonlinear components show higher degree of consistency in their post-landfall behavior across the estuary. This coherence is evident in the post-landfall nTSI and nTWI KDEs (cyan lines), that exhibit overlapping distributions with similar spread across stations suggesting a relatively consistent mode of nonlinear response under differing storm conditions. Although their distribution peaks remain in the negative range consistent with an overall dampening effect, positive nonlinear amplification becomes increasingly apparent, particularly at the mid-bay (LEW: Fig. 10k, q) and upper-bay (ANN: Fig. 10l, r) stations. In contrast, nTSI and nTWI maintain a predominantly negative response in the lower bay (KK: Fig. 10j, p), where it helps accelerate residual surge dissipation. For Hurricane Irene, nTWI acts counter to the TWI+WW response, which shows a strong dampening effect ranging from –0.65 m to –0.15 m (Fig. 10g–i), while nTWI peaks positively between +0.025 m and +0.075 m (Fig. 10p–r) highlighting the compensatory role of NI during the post-landfall phase. As for nTRI Fig. 10m-o shows a clear positive signature in the upper bay, reaching up to +0.045 m at ANN, and is tied to delayed runoff effects following Sandy and Isabel.

5. Conclusion

In this study, we set up, calibrated, and validated coastal hydrodynamic and wave models to analyze the spatiotemporal characteristics of annual and tropical cyclone-induced nonlinear interactions among tides, storm surge, wind-induced waves, and river flow in the Chesapeake Bay, USA. The models helped design five simulation scenarios to isolate the individual and combined effects of NIs among tides, storm surge, river discharge, and wind-induced waves. The calibration and validation process confirmed the models' strong predictive skill. Performance metrics indicate that the model effectively captures both the phase and amplitude of extreme water levels, with minor discrepancies attributed to biases in wind field data.

Annual NIs and inherent total interaction exhibits substantial variability, with extreme hurricanes triggering abrupt and spatially diverse responses. In slow-moving hurricanes, the inverse barometer effect has a considerable influence on the system's response due to sustained low-pressure conditions. On the other hand, fast-moving hurricanes with strong wind fields are dominated by wind-driven setup that dictates the system's response. In the pre-landfall stage, the combined effect of TSI+SS and TWI+WW are predominantly negative reflecting early influences of positive pressure anomalies and offshore winds. At landfall, these interactions have a relatively consistent spread in the lower bay. In contrast, the middle and upper bays exhibit greater variability indicating heightened sensitivity to storm-specific forcings.

Across storms, the post-landfall stage shows a recurring out-of-phase pattern with the dominant surge and wind effects. Therefore, a weak or neutral tide–driver interaction does suggest a negligible NI impact. In fact, nonlinear effects (nTSI, nTWI) generally oppose the tide–driver interactions they stem from, acting as compensatory forces that modulate extreme water levels through amplification or suppression. Spatially, the NIs are transient and of high frequency near the coast, but exhibit slower, more persistent fluctuations in upstream regions. During landfall, nTSI shows a highly dynamic response in the lower bay, but its signal weakens upstream as transitions into a predominantly dampening phase. In contrast, nTWI shows minimal spatial attenuation and maintains a consistent signal across all stations. These findings show that while tide–driver interactions and nonlinear effects are storm-specific and stage-dependent, they exhibit recurring spatiotemporal patterns across the estuarine system. Therefore, despite contrasting storm dynamics (e.g., intensity, track, translational speed), the estuary exhibits consistent stage-wise signatures: pre-landfall drawdown, peak nonlinear response at landfall, and post-landfall out-of-phase nonlinearity.

Data and materials availability

Delft3D 4.04.01 (e.g., FLOW, WAVE) is an open-source hydrodynamic modeling software released under the GNU General Public License (GPL) and can be downloaded from https://oss.deltares.nl/web/

delft3d/. SWAN is fully open source under the GPL and can be downloaded from https://www.swan.tudelft.nl/downloads/. Links to data repositories and archives for digital elevation models (DEMs), land cover data, and boundary forcings (including water levels and river discharges) are provided throughout the manuscript. Meteorological data: https://cds.climate.copernicus.eu/ and https://www.hycom.org/dataserver/ncep-cfsv2.

CRediT authorship contribution statement

Md Shadman Sakib: Writing – original draft, Visualization, Validation, Software, Methodology, Investigation, Formal analysis, Data curation, Conceptualization. **David F. Muñoz:** Writing – review & editing, Supervision, Resources, Project administration, Methodology, Investigation, Funding acquisition, Conceptualization. **Thomas Wahl:** Writing – review & editing.

Declaration of competing interest

The authors declare that they have no known competing financial interests or personal relationships that could have appeared to influence the work reported in this paper.

Funding and acknowledgments

D.F.M acknowledges partial financial support from the U.S. National Science Foundation (NSF), CAS-Climate Program (Award # 480948). T. W. acknowledges support from the U.S. NSF (Award # 2141461) and the NASA Sea Level Change Team (Award # 80NSSC24K1527).

Supplementary materials

Supplementary material associated with this article can be found, in the online version, at doi:10.1016/j.advwatres.2025.105108.

Data availability

I have shared the links with all available data and open source models used in this study.

References

Bakhtyar, R., Maitaria, K., Velissariou, P., Trimble, B., Mashriqui, H., Moghimi, S., Abdolali, A., Van Der Westhuysen, A.J., Ma, Z., Clark, E.P., Flowers, T., 2020. A new 1D/2D coupled modeling approach for a riverine-estuarine system under storm events: application to Delaware River Basin. J. Geophys. Res. 125 (9), e2019JC015822. https://doi.org/10.1029/2019JC015822.

Battjes, J.A., Janssen, J.P.F.M., 1978. Energy loss and set-up due to breaking of random waves. Coast. Eng. 1978, 569–587. https://doi.org/10.1061/9780872621909.034.

Bennett, V.C.C., Mulligan, R.P., Hapke, C.J., 2018. A numerical model investigation of the impacts of Hurricane Sandy on water level variability in Great South Bay, New York. Cont. Shelf Res. 161, 1–11. https://doi.org/10.1016/j.csr.2018.04.003.

Bernier, N.B., Thompson, K.R., 2007. Tide-surge interaction off the east coast of Canada and northeastern United States. J. Geophys. Res. 112 (C6), 2006JC003793. https://doi.org/10.1029/2006JC003793.

Beven, J., & Cobb, H. (2003). *Tropical cyclone report Hurricane Isabel.*

Bilskie, M.V., Hagen, S.C., 2018. Defining flood zone transitions in low-gradient coastal regions. Geophys. Res. Lett. 45 (6), 2761–2770. https://doi.org/10.1002/2018GL077524.

Blake, E., Kimberlain, T., Berg, R., Cangialosi, J., & Beven, J. (2012). *Tropical cyclone report Hurricane Sandy (AL182012)*. https://www.nhc.noaa.gov/data/tcr/AL182012_Sandy.pdf.

Bolaños, R., Brown, J.M., Amoudry, L.O., Souza, A.J., 2013. Tidal, riverine, and wind influences on the circulation of a macrotidal estuary. J. Phys. Oceanogr. 43 (1), 29–50. https://doi.org/10.1175/JPO-D-11-0156.1.

Cai, H., Savenije, H.H.G., Toffolon, M., 2014. Linking the river to the estuary: influence of river discharge on tidal damping. Hydrol. Earth. Syst. Sci. 18 (1), 287–304. https://doi.org/10.5194/hess-18-287-2014.

Cai, H., Savenije, H.H.G., Garel, E., Zhang, X., Guo, L., Zhang, M., Liu, F., Yang, Q., 2019. Seasonal behaviour of tidal damping and residual water level slope in the Yangtze River estuary: identifying the critical position and river discharge for maximum tidal damping. Hydrol. Earth. Syst. Sci. 23 (6), 2779–2794. https://doi.org/10.5194/hess-23-2779-2019.

Chen, W.-B., Lin, L.-Y., Jang, J.-H., Chang, C.-H., 2017. Simulation of typhoon-induced storm tides and wind waves for the northeastern coast of Taiwan using a tide–surge–wave coupled model. Water 9 (7), 549. https://doi.org/10.3390/w9070549.

Colman, S.M., Mixon, R.B., 1988. The record of major quaternary sea-level changes in a large coastal plain estuary, Chesapeake Bay, Eastern United States. Palaeogeogr. Palaeoclimatol. Palaeoecol. 68 (2–4), 99–116. https://doi.org/10.1016/0031-0182(88)90033-8.

Deb, M., Sun, N., Yang, Z., Wang, T., Judi, D., Xiao, Z., Wigmosta, M.S., 2023. Interacting effects of watershed and coastal processes on the evolution of compound flooding during Hurricane Irene. Earth's Fut. 11 (3), e2022EF002947. https://doi.org/10.1029/2022EF002947.

Deltares. (2018a). *Delft3D-FLOW user Manual.*

Deltares. (2018b). *Delft3D-WAVE user Manual.*

Deltares. (2023). *D-Flow Flexible mesh user Manual.*

Dietrich, J.C., Bunya, S., Westerink, J.J., Ebersole, B.A., Smith, J.M., Atkinson, J.H., Jensen, R., Resio, D.T., Luettich, R.A., Dawson, C., Cardone, V.J., Cox, A.T., Powell, M.D., Westerink, H.J., Roberts, H.J., 2010. A high-resolution coupled riverine flow, tide, wind, wind wave, and storm surge model for southern Louisiana and Mississippi. Part II: synoptic description and analysis of Hurricanes Katrina and Rita. Mon. Weather. Rev. 138 (2), 378–404. https://doi.org/10.1175/2009MWR2907.1.

Dronkers, J., 1986. Tidal asymmetry and estuarine morphology. Netherlands J. Sea Res. 20 (2–3), 117–131. https://doi.org/10.1016/0077-7579(86)90036-0.

Elahi, M.W.E., Jalón-Rojas, I., Wang, X.H., Ritchie, E.A., 2020. Influence of seasonal river discharge on tidal propagation in the Ganges-Brahmaputra-Meghna Delta, Bangladesh. J. Geophys. Res. Oceans 125 (11), e2020JC016417. https://doi.org/10.1029/2020JC016417.

Fagherazzi, S., Wiberg, P.L., Howard, A.D., 2003. Tidal flow field in a small basin. J. Geophys. Res. 108 (C3), 2002JC001340. https://doi.org/10.1029/2002JC001340.

Feng, J., Li, D., Li, Y., Liu, Q., Wang, A., 2018. Storm surge variation along the coast of the Bohai Sea. Sci. Rep. 8 (1), 11309. https://doi.org/10.1038/s41598-018-29712-z.

Funakoshi, Y., Hagen, S.C., Bacopoulos, P., 2008. Coupling of hydrodynamic and wave models: case study for Hurricane Floyd (1999) hindcast. J. Waterw. Port. Coast. Ocean. Eng. 134 (6), 321–335. https://doi.org/10.1061/(ASCE)0733-950X(2008)134:6(321).

Glahn, B., Taylor, A., Kurkowski, N., Shaffer, W.A., 2009. The role of the SLOSH model in National Weather Service storm surge forecasting. Natl. Weather Digest 33, 3–14.

Green, J., Haigh, I.D., Quinn, N., Neal, J., Wahl, T., Wood, M., Eilander, D., De Ruiter, M., Ward, P., Camus, P., 2025. Review article: a comprehensive review of compound flooding literature with a focus on coastal and estuarine regions. Nat. Hazards Earth Syst. Sci. 25 (2), 747–816. https://doi.org/10.5194/nhess-25-747-2025.

Guo, L., Van Der Wegen, M., Jay, D.A., Matte, P., Wang, Z.B., Roelvink, D., He, Q., 2015. River-tide dynamics: exploration of nonstationary and nonlinear tidal behavior in the Y angtze R iver estuary. J. Geophys. Res. 120 (5), 3499–3521. https://doi.org/10.1002/2014JC010491.

Höffken, J., Vafeidis, A.T., MacPherson, L.R., Dangendorf, S., 2020. Effects of the temporal variability of storm surges on coastal flooding. Front. Mar. Sci. 7, 98. https://doi.org/10.3389/fmars.2020.00098.

Haase, A., Wang, J., Taylor, A., & Feyen, J. (2012). Coupling of tides and storm surge for operational modeling on the Florida coast. *Estuarine and Coastal Modeling*, 230–238. doi:10.1061/9780784412411.00014.

Haigh, I.D., Wahl, T., Rohling, E.J., Price, R.M., Pattiaratchi, C.B., Calafat, F.M., Dangendorf, S., 2014. Timescales for detecting a significant acceleration in sea level rise. Nat. Commun. 5, 3635. https://doi.org/10.1038/ncomms4635.

Hasan Tanim, A., Goharian, E., 2021. Developing a hybrid modeling and multivariate analysis framework for storm surge and runoff interactions in urban coastal flooding. J. Hydrol. 595, 125670. https://doi.org/10.1016/j.jhydrol.2020.125670.

Hasselmann, K., Barnett, T., Carlson, E., Cartwright, H., Enke, D., Ewing, K., Gienapp, H., Hasselmann, D., Kruseman, P., Meerburg, A., Müller, P., Olbers, D., Richter, K., Sell, W., Walden, H., 1973. Measurements of wind-wave growth and swell decay during the Joint North Sea Wave Project (JONSWAP). Deutsche Hydrographische Zeitschrift 12 (A8), 95.

Horsburgh, K.J., Wilson, C., 2007. Tide-surge interaction and its role in the distribution of surge residuals in the North Sea. J. Geophys. Res. 112 (C8), 2006JC004033. https://doi.org/10.1029/2006JC004033.

Huang, L., Zhang, T., Zhang, S., & Wang, H. (2024). *Effect of nonlinear tide-surge interaction in the Pearl River Estuary during Typhoon Nida (2016)*. doi:10.5194/egusphere-2024-1940.

Jiang, P., Yu, Z., Gautam, M.R., Yuan, F., Acharya, K., 2016. Changes of storm properties in the United States: observations and multimodel ensemble projections. Glob. Planet. Change 142, 41–52. https://doi.org/10.1016/j.gloplacha.2016.05.001.

Kästner, K., Hoitink, A.J.F., Torfs, P.J.J.F., Deleersnijder, E., Ningsih, N.S., 2019. Propagation of tides along a river with a sloping bed. J. Fluid Mech. 872, 39–73. https://doi.org/10.1017/jfm.2019.331.

Kerns, B.W., Chen, S.S., 2023. Inland flooding and rainfall from Hurricane Irene and Tropical Storm Lee (2011): coupled atmosphere–Wave–Ocean model simulations and remote sensing and In situ observations with a machine learning tool. Weather. Forecast. 38 (5), 677–697. https://doi.org/10.1175/WAF-D-22-0100.1.

Komen, G.J., Hasselmann, S., Hasselmann, K., 1984. On the existence of a fully developed wind-sea spectrum. J. Phys. Oceanogr. 14 (8), 1271–1285. https://doi.org/10.1175/1520-0485(1984)014<1271:OTEOAF>2.0.CO;2.

Kumar, M., Bhatt, G., Duffy, C.J., 2009. An efficient domain decomposition framework for accurate representation of geodata in distributed hydrologic models. Int. J. Geogr. Inf. Sci. 23 (12), 1569–1596. https://doi.org/10.1080/13658810802344143.
Li, X., Fu, D., Nielsen-Gammon, J., Gangrade, S., Kao, S.-C., Chang, P., Morales Hernández, M., Voisin, N., Zhang, Z., Gao, H., 2023. Impacts of climate change on future hurricane induced rainfall and flooding in a coastal watershed: a case study on Hurricane Harvey. J. Hydrol. 616, 128774. https://doi.org/10.1016/j.jhydrol.2022.128774.
Lin, N., Smith, J.A., Villarini, G., Marchok, T.P., Baeck, M.L., 2010. Modeling extreme rainfall, winds, and surge from Hurricane Isabel (2003). Weather. Forecast. 25 (5), 1342–1361. https://doi.org/10.1175/2010WAF2222349.1.
Lixion, A., Cangialosi, J., 2011. Tropical Cyclone Report Hurricane Irene (AL092011). National Hurricane Center. https://nhc.noaa.gov/data/tcr/AL092011_Irene.pdf.
Losada, M.A., Díez-Minguito, M., Reyes-Merlo, M.Á., 2017. Tidal-fluvial interaction in the Guadalquivir River Estuary: Spatial and frequency-dependent response of currents and water levels: Tidal-fluvial interaction in the GRE. J. Geophys. Res. Oceans 122 (2), 847–865. https://doi.org/10.1002/2016JC011984.
Lyddon, C., Brown, J.M., Leonardi, N., Plater, A.J., 2018. Uncertainty in estuarine extreme water level predictions due to surge-tide interaction. PLoS. One 13 (10), e0206200. https://doi.org/10.1371/journal.pone.0206200.
Marsooli, R., Lin, N., 2018. Numerical modeling of historical storm tides and waves and their interactions along the U.S. East and Gulf Coasts. J. Geophys. Res. Oceans 123 (5), 3844–3874. https://doi.org/10.1029/2017JC013434.
Moftakhari, H.R., Salvadori, G., AghaKouchak, A., Sanders, B.F., Matthew, R.A., 2017. Compounding effects of sea level rise and fluvial flooding. Proc. Natl. Acad. Sci. 114 (37), 9785–9790. https://doi.org/10.1073/pnas.1620325114.
Muñoz, D.F., Moftakhari, H., Moradkhani, H., 2020. Compound effects of flood drivers and wetland elevation correction on Coastal flood hazard assessment. Water Resour. Res. 56 (7), e2020WR027544. https://doi.org/10.1029/2020WR027544.
Muñoz, D.F., Yin, D., Bakhtyar, R., Moftakhari, H., Xue, Z., Mandli, K., Ferreira, C., 2022. Inter-model comparison of Delft3D-FM and 2D HEC-RAS for total water level prediction in coastal to inland transition zones. JAWRA J. Am. Water Resour. Assoc. 58 (1), 34–49. https://doi.org/10.1111/1752-1688.12952.
Muñoz, D.F., Moftakhari, H., Moradkhani, H., 2024. Quantifying cascading uncertainty in compound flood modeling with linked process-based and machine learning models. Hydrol. Earth. Syst. Sci. 28 (11), 2531–2553. https://doi.org/10.5194/hess-28-2531-2024.
Mulligan, R.P., Hay, A.E., Bowen, A.J., 2008. Wave-driven circulation in a coastal bay during the landfall of a hurricane. J. Geophys. Res. 113 (C5), 2007JC004500. https://doi.org/10.1029/2007JC004500.
Mulligan, R.P., Walsh, J.P., Wadman, H.M., 2015. Storm surge and surface waves in a shallow lagoonal estuary during the crossing of a hurricane. J. Waterw. Port. Coast. Ocean. Eng. 141 (4), A5014001. https://doi.org/10.1061/(ASCE)WW.1943-5460.0000260.
Nadal-Caraballo, N.C., Melby, J.A., Gonzalez, V.M., Cox, A.T., 2015. *North Atlantic Coast Comprehensive Study (NACCS): Coastal storm Hazards from Virginia to Maine* (No. ERDC/CHL TR-15-5). U.S. Army Engineer Research and Development Center (Coastal and Hydraulics Laboratory). https://www.nad.usace.army.mil/Portals/40/docs/ComprehensiveStudy/Coastal_Storm_Hazards_from_Virginia_to_Maine.pdf.
NOAA, 2004a. Effects Of Hurricane Isabel On Water Levels Data Report. National Oceanic and Atmospheric Administration, p. 132. https://tidesandcurrents.noaa.gov/publications/techrpt40.pdf.
NOAA. (2004b). *National Weather Service service assessment: hurricane Isabel*.
NOAA, 2012. Monthly National Climate Report foroctober 2012. National Centers for Environmental Information. https://www.ncei.noaa.gov/access/monitoring/monthly-report/national/201210.
OrtizBeviá, M.J., Pérez-González, I., Alvarez-García, F.J., Gershunov, A., 2010. Nonlinear estimation of El Niño impact on the North Atlantic winter. J. Geophys. Res. Atmos. 115 (D21), 2009JD013387. https://doi.org/10.1029/2009JD013387.
Patrick, R., 1994. Rivers of the United States, Vol. 1: Estuaries, 1. John Wiley and Sons.
Penny, A.B., Alaka, L., Taylor, A.A., Booth, W., DeMaria, M., Fritz, C., Rhome, J., 2023. Operational Storm surge forecasting at the National Hurricane Center: the case for probabilistic guidance and the evaluation of improved storm size forecasts used to define the wind forcing. Weather. Forecast. 38 (12), 2461–2479. https://doi.org/10.1175/WAF-D-22-0209.1.
Pinheiro, J.P., Lopes, C.L., Ribeiro, A.S., Sousa, M.C., Dias, J.M., 2020. Tide-surge interaction in Ria de Aveiro lagoon and its influence in local inundation patterns. Cont. Shelf Res. 200, 104132. https://doi.org/10.1016/j.csr.2020.104132.
Preller, R.H., Posey, P.G., & Dawson, G.M. (2003). *Hurricane Isabel: a numerical model study of storm surge along The East coast of The United States*.
Ralston, D.K., Talke, S., Geyer, W.R., Al-Zubaidi, H.A.M., Sommerfield, C.K., 2019. Bigger tides, less flooding: effects of dredging on barotropic dynamics in a highly modified estuary. J. Geophys. Res. 124 (1), 196–211. https://doi.org/10.1029/2018JC014313.
Reed, A.J., Mann, M.E., Emanuel, K.A., Lin, N., Horton, B.P., Kemp, A.C., Donnelly, J.P., 2015. Increased threat of tropical cyclones and coastal flooding to New York City during the anthropogenic era. Proc. Natl. Acad. Sci. 112 (41), 12610–12615. https://doi.org/10.1073/pnas.1513127112.
Roberts, K.J., Pringle, W.J., Westerink, J.J., 2019. OceanMesh2D 1.0: MATLAB-based software for two-dimensional unstructured mesh generation in coastal ocean modeling. Geosci. Model. Dev. 12 (5), 1847–1868. https://doi.org/10.5194/gmd-12-1847-2019.
Sarhadi, A., Rousseau-Rizzi, R., Mandli, K., Neal, J., Wiper, M.P., Feldmann, M., Emanuel, K., 2024. Climate change contributions to increasing compound flooding risk in New York City. Bull. Am. Meteorol. Soc. 105 (2), E337–E356. https://doi.org/10.1175/BAMS-D-23-0177.1.
Sassi, M.G., Hoitink, A.J.F., 2013. River flow controls on tides and tide-mean water level profiles in a tidal freshwater river. J. Geophys. Res. 118 (9), 4139–4151. https://doi.org/10.1002/jgrc.20297.
Semedo, A., Weisse, R., Behrens, A., Sterl, A., Bengtsson, L., Günther, H., 2012. Projection of global wave climate change toward the end of the twenty-first century. J. Clim. 26 (21), 8269–8288. https://doi.org/10.1175/JCLI-D-12-00658.1.
Serafin, K.A., Ruggiero, P., Stockdon, H.F., 2017. The relative contribution of waves, tides, and nontidal residuals to extreme total water levels on U.S. West Coast sandy beaches. Geophys. Res. Lett. 44 (4), 1839–1847. https://doi.org/10.1002/2016GL071020.
Smith, S.D., Banke, E.G., 1975. Variation of the sea surface drag coefficient with wind speed. Q. J. R. Meteorol. Soc. 101 (429), 665–673. https://doi.org/10.1002/qj.49710142920.
Smith, A.B., 2025. U.S. Billion-dollar Weather and Climate Disasters, 1980—Present (NCEI Accession 0209268). NOAA National Centers for Environmental Information. https://doi.org/10.25921/STKW-7W73 [Dataset].
Tang, Y.M., Sanderson, B., Holland, G., Grimshaw, R., 1996. A numerical study of storm surges and tides, with application to the North Queensland Coast. J. Phys. Oceanogr. 26 (12), 2700–2711. https://doi.org/10.1175/1520-0485(1996)026<2700:ANSOSS>2.0.CO;2.
Tien, P.V., Thuy, N.B., Kim, S., Cuong, N.K., Ngoc, P.K., Khiem, M.V., Hole, L.R., 2025. Impact of the interaction of surge, wave, and tide on the surge and wave on the northern coast of Vietnam for a marine storm surge and wave forecast system. Reg. Stud. Mar. Sci. 87, 104234. https://doi.org/10.1016/j.rsma.2025.104234.
Tolkova, E., Tang, L., Riley, J., Jeong, I., & White, S. (2023). *VDatum update for Chesapeake Bay, Delaware Bay, and adjacent waters: tidal datums, sea surface topography, and their spatially varying uncertainties*.
Valle-Levinson, A., Li, C., Wong, K., Lwiza, K.M.M., 2000. Convergence of lateral flow along a coastal plain estuary. J. Geophys. Res. 105 (C7), 17045–17061. https://doi.org/10.1029/2000JC900025.
Vitousek, S., Barnard, P.L., Fletcher, C.H., Frazer, N., Erikson, L., Storlazzi, C.D., 2017. Doubling of coastal flooding frequency within decades due to sea-level rise. Sci. Rep. 7 (1), 1399. https://doi.org/10.1038/s41598-017-01362-7.
Węglarczyk, S., 2018. Kernel density estimation and its application. In: ITM Web of Conferences, 23, 00037. https://doi.org/10.1051/itmconf/20182300037.
Wankang, Y., Baoshu, Y., Xingru, F., Dezhou, Y., Guandong, G., Haiying, C., 2019. The effect of nonlinear factors on tide-surge interaction: a case study of Typhoon Rammasun in Tieshan Bay, China. Estuar. Coast. Shelf Sci. 219, 420–428. https://doi.org/10.1016/j.ecss.2019.01.024.
Wijetunge, J.J., Neluwala, N.G.P.B., 2023. Compound flood hazard assessment and analysis due to tropical cyclone-induced storm surges, waves and precipitation: a case study for coastal lowlands of Kelani river basin in Sri Lanka. Nat. Hazards 116 (3), 3979–4007. https://doi.org/10.1007/s11069-023-05846-w.
Xiao, Z., Yang, Z., Wang, T., Sun, N., Wigmosta, M., Judi, D., 2021. Characterizing the non-linear interactions between tide, storm surge, and river flow in the Delaware Bay Estuary, United States. Front. Mar. Sci. 8, 715557. https://doi.org/10.3389/fmars.2021.715557.
Xing, J., Davies, A.M., Jones, J.E., 2012. Influence of sea surface wind wave turbulence upon wind-induced circulation, tide–surge interaction and bed stress. Ocean Dyn 62 (7), 1017–1042. https://doi.org/10.1007/s10236-012-0542-8.
Xiong, Y., Berger, C.R., 2010. Chesapeake Bay tidal characteristics. J. Water Resource Prot. 02 (07), 619–628. https://doi.org/10.4236/jwarp.2010.27071.
Xu, D., Bisht, G., Engwirda, D., Feng, D., Tan, Z., Ivanov, V.Y., 2025. Uncertainties in simulating flooding during Hurricane Harvey using 2D shallow water equations. Water Resour. Res. 61 (1), e2024WR038032. https://doi.org/10.1029/2024WR038032.
Yin, D., Muñoz, D.F., Bakhtyar, R., Xue, Z.G., Moftakhari, H., Ferreira, C., Mandli, K., 2022. Extreme water level simulation and component analysis in Delaware Estuary during Hurricane Isabel. JAWRA J. Am. Water Resour. Assoc. 58 (1), 19–33. https://doi.org/10.1111/1752-1688.12947.
Zheng, J., Wang, J., Zhou, C., Zhao, H., Sang, S., 2017. Numerical simulation of typhoon-induced storm surge along Jiangsu coast, part II: calculation of storm surge. Water Sci. Eng. 10 (1), 8–16. https://doi.org/10.1016/j.wse.2017.03.011.
Zheng, P., Li, M., Wang, C., Wolf, J., Chen, X., De Dominicis, M., Yao, P., Hu, Z., 2020. Tide-surge interaction in the Pearl River Estuary: a case study of Typhoon Hato. Front. Mar. Sci. 7, 236. https://doi.org/10.3389/fmars.2020.00236.
Zhong, L., Li, M., 2006. Tidal energy fluxes and dissipation in the Chesapeake Bay. Cont. Shelf Res. 26 (6), 752–770. https://doi.org/10.1016/j.csr.2006.02.006.
Zscheischler, J., Martius, O., Westra, S., Bevacqua, E., Raymond, C., Horton, R.M., Van Den Hurk, B., AghaKouchak, A., Jézéquel, A., Mahecha, M.D., Maraun, D., Ramos, A.M., Ridder, N.N., Thiery, W., Vignotto, E., 2020. A typology of compound weather and climate events. Nat. Rev. Earth Environ. 1 (7), 333–347. https://doi.org/10.1038/s43017-020-0060-z.